

Atmospheric pollution from rockets

Ioannis W. Kokkinakis^{1, a)} and Dimitris Drikakis^{1, b)}
University of Nicosia, Nicosia CY-2417, Cyprus

(Dated: 26 March 2022)

We address the impact of rockets exhaust gases on atmospheric pollution through high-resolution computational fluid dynamics simulations. We have modeled the exhaust gases and developing plume at several altitudes along a typical trajectory of a standard present-day rocket, as a prototypical example of a two-stage rocket to transport people and payloads into Earth orbit and beyond. The modeled rocket uses RP-1 as the propellant and liquid oxygen (LOx) as the oxidizer to generate $\sim 6,806$ kN of thrust via a total of 9 nozzles, matching –as closely as possible based on available data– the specifications to the Thaicom 8 launch mission of the Falcon 9 rocket manufactured by SpaceX. We have used high-order discretization methods, 11th-order accurate, in conjunction with Implicit Large Eddy Simulations to model exhaust gas mixing, dispersion, and heat transfer into the atmosphere at altitudes up to 67 km. We show that pollution from rockets should not be underestimated as frequent future rocket launches could have a significant cumulative effect on climate. The production of thermal nitrogen oxides (NOx) can remain considerable up to altitudes with an ambient atmospheric pressure below but of the same order of magnitude as the nozzles exit pressure. At the same time, the emitted mass of carbon dioxide (CO₂) in the mesosphere is equivalent to that contained in 26 cubic kilometers of atmospheric air at the same altitude.

I. INTRODUCTION

Commercial space flights will continue to rise as reusable space vehicle technology will allow space transportation at a low cost. This is also evident by the recent flights of SpaceX, Virgin Galactic, and the New Shepard space ships.

Past studies have shown that rocket launches could significantly contribute to atmospheric pollution considering the pace of growth in space flights. They have suggested careful investigation of rocket propellant types, including kerosene-fueled and solid rocket motors, including research into the gases and particles emitted into the middle and upper atmosphere that could change atmospheric radiation patterns^{1,2}. Experts have stated and emphasized that the impact of rockets on climate has not been seriously addressed³. However, we know that accumulated effects can heat the upper stratosphere, leading to ozone loss. The rockets propulsion creates significant heating in the atmosphere, which is poorly (if not at all) understood. We speculate that the limited research on this topic is because rocket launches presently have a negligible effect on total stratospheric ozone⁴. However, we should expect that rocket emissions will increase more significantly than currently due to the developments in the space industry. Therefore, the impact on the atmosphere will be a crucial factor requiring careful consideration in the design of future rocket launches.

The issue of rocket emissions affecting the middle and upper atmosphere was included in the United Nations 2018 Quadrennial Global Ozone Assessment⁴. We envisage that the forthcoming 2022 World Meteorological Organization (WMO) and United Nations Environment Programme (UNEP) Ozone Assessment will also contain the most up-to-date understanding of ozone depletion from rockets emissions, amongst other factors. The 2018 UN report and fur-

ther published research highlighted that existing model predictions are incomplete and microphysical parameters, such as the emitted alumina particles distribution and the chlorine activation rate constant, are not well understood. The models should account for the different types of rocket fuels/propellants and research on their impact on atmospheric radiation and chemistry is scarce. Microphysical parameters, such as the emitted alumina particles distribution and the chlorine activation rate constant, need further investigation. The above are considered essential because alumina-related global ozone loss could be tenfold more significant than presently assumed⁵. All the above could have longer-term implications for the earth's climate.

Improved understanding of rocket emissions requires modeling and simulation of fluid dynamics of rocket exhaust gases into the atmosphere, atmospheric chemistry changes due to gas emissions from rockets, and a better appreciation of the effects of different fuels/propellants. The insight into the gas dispersion into the atmosphere is crucial for appreciating the scale of pollution. The above motivated the present research.

This paper focuses on the dispersion of exhaust gases from a rocket, taking as a prototypical example, the Falcon 9 of SpaceX. The selection was based on data availability of exhaust gases rather than a choice of preference. We present computational fluid dynamics (CFD) simulations of the exhaust gas emissions, mixing and dispersion into the atmosphere for distances up to 1 km from the nozzle orifices and altitudes up to 67 km. Specifically, we have performed implicit large eddy simulation (ILES) in conjunction with very high-order methods that significantly increase the accuracy on coarser mesh CFD simulations^{6–11}, in general, and in turbulent simulations in particular,^{12–20}.

The objectives of our study are:

- To develop a high-order CFD simulation framework for studying rockets exhaust plumes.
- To investigate the immediate mixing and heat-transfer of the combustion by-products for altitudes up to 67 km into the atmosphere.

^{a)}Electronic mail: kokkinakis.i@unic.ac.cy

^{b)}Electronic mail: drikakis.d@unic.ac.cy

- To assess the potential impact of a rocket launch on atmospheric pollution.
- To stimulate future studies into the above topics that research is still in its infancy.

II. COMPUTATIONAL METHODOLOGY

We solve the compressible Navier-Stokes equations (NSE) for an ideal gas using the finite volume method (FVM). In integral form, the NSE are formulated as follows:

Mass-conservation,

$$\frac{\partial}{\partial t} \iiint_V \rho dV = - \oint_A \rho (\mathbf{u} \cdot \hat{\mathbf{n}}) dA \quad (1)$$

Momentum-conservation,

$$\begin{aligned} \frac{\partial}{\partial t} \iiint_V \rho \mathbf{u} dV = & - \oint_A \rho \mathbf{u} (\mathbf{u} \cdot \hat{\mathbf{n}}) dA - \oint_A p \hat{\mathbf{n}} dA \\ & + \oint_A \boldsymbol{\tau} \cdot \hat{\mathbf{n}} dA + \iiint_V \rho \mathbf{f}_b dV \end{aligned} \quad (2)$$

Total energy conservation,

$$\begin{aligned} \frac{\partial}{\partial t} \iiint_V \rho e_t dV = & - \oint_A \rho e_t (\mathbf{u} \cdot \hat{\mathbf{n}}) dA - \oint_A p (\mathbf{u} \cdot \hat{\mathbf{n}}) dA \\ & + \oint_A (\mathbf{u} \cdot \boldsymbol{\tau}) \cdot \hat{\mathbf{n}} dA - \oint_A (\mathbf{q}_c + \mathbf{q}_d) \cdot \hat{\mathbf{n}} dA \\ & + \iiint_V \rho (\mathbf{f}_b \cdot \mathbf{u}) dV \end{aligned} \quad (3)$$

Species mass conservation,

$$\frac{\partial}{\partial t} \iiint_V \rho y_j dV = - \oint_A \rho y_j (\mathbf{u} \cdot \hat{\mathbf{n}}) dA + \oint_A (\mathbf{J}_j \cdot \hat{\mathbf{n}}) dA \quad (4)$$

where ρ is the density; \mathbf{u} is the velocity vector; p is the static pressure; $\hat{\mathbf{n}}$ is the outward pointing unit normal of a surface element dA of the closed finite control volume dV ; \mathbf{f}_b is an external body force; y_j is the mass-fraction of the j -th species; e_t is the total energy per unit mass given by $e_t = e + \mathbf{u} \cdot \mathbf{u}/2$; e is the specific internal energy. Furthermore, we denote T the temperature, c_v the specific heat capacity at constant volume, and γ the heat capacity ratio ($\gamma = c_p/c_v$) where c_p is the specific heat capacity at constant pressure.

For a Newtonian fluid, the shear stress tensor is given by,

$$\boldsymbol{\tau} = \lambda (\nabla \cdot \mathbf{u}) \mathbf{I} + \mu [\nabla \otimes \mathbf{u} + (\nabla \otimes \mathbf{u})^T] \quad (5)$$

where \mathbf{I} is the identity tensor; the second coefficient of viscosity is given by $\lambda = -2\mu/3$ according to Stoke's hypothesis; and μ is the dynamic viscosity.

The heat flux is calculated by Fourier's Law of heat conduction,

$$\mathbf{q}_c = -\kappa \nabla T \quad (6)$$

where κ is the heat conductivity.

The species diffusional fluxes are commonly computed via the Fickian (gradient) diffusion approximation,

$$\mathbf{J}_j = \rho D_j \nabla y_j \quad (7)$$

where D_j is an effective binary species diffusion coefficient.

Finally, the inter-diffusional enthalpy flux, \mathbf{q}_d is given by,

$$\mathbf{q}_d = - \sum_{i=1}^{N_{sp}} h_i \mathbf{J}_i \quad (8)$$

where the enthalpy of each individual j -th species is defined by $h_j = e_j + p_j/\rho_j$.

A. Thermodynamics

We assume a thermally perfect gas with the species-specific heats being a function of temperature. The specific heats are calculated using a fourth-order polynomial in the fluid temperature interval 300–5,000 K. The same polynomial form is utilized of all species but with different coefficients specific to each species.

The functional form for the standard-state specific heat capacity at constant pressure is a fourth-order polynomial:

$$\frac{C_{pm,j}}{R_u} = \sum_{n=1}^N a_{nj} T^{(n-1)}, \quad (9)$$

where $C_{pm,j}$ is the molar heat capacity at constant pressure of the j -th species. The approximation $C_{pm,j}(T)$ is considered for two temperature ranges for each of which seven coefficients a_j are needed. According to Eq. (9), these polynomial approximations take the following form,

$$\frac{C_{pm,j}}{R_u} = a_{1j} + a_{2j}T + a_{3j}T^2 + a_{4j}T^3 + a_{5j}T^4, \quad (10)$$

where the (absolute) temperature is in Kelvin. The j -th species specific heat capacity at constant pressure is obtained according to $c_{p,j} = C_{pm,j}/\mathcal{M}_j$, where \mathcal{M}_j is the molar mass of the j -th species. The mixture value, c_p , is then calculated by $c_p = \sum_j c_{p,j} y_j$.

The mixture heat capacity ratio, γ , is then calculated according to the formula for an ideal gas,

$$\gamma(y, T) = c_p / (c_p - R_*), \quad (11)$$

where $R_* = \sum_j R_{*,j} y_j$ is the mixture's specific gas constant. Therefore, the mixture γ is a function of both the temperature, T , and the composition, $\sum_j y_j$.

Using the ideal gas equation of state, the temperature and pressure can be obtained from the internal energy

$$e = \frac{p}{\rho(\gamma - 1)} = c_v T, \quad (12)$$

For an ideal gas, the specific heat capacity at constant volume is given by $c_v = c_p/\gamma$.

B. Numerical methods

We have employed iLES in the framework of the CFD code CNS3D^{6,20}. A detailed description of the method can be found in the recent study by Kokkinakis et al.²⁰. The code solves the Navier-Stokes equations using a finite volume Godunov-type method for the convective terms. We discretize the inter-cell numerical fluxes by solving the Riemann problem using the reconstructed values of the primitive variables at the cell interfaces. We use a one-dimensional swept unidirectional stencil for the reconstruction of the variables. The Riemann problem is solved using the “Harten, Lax, van Leer, and (the missing) Contact” (HLLC) approximate Riemann solver^{21,22}. The high-order numerical discretization is based on an 11th-order Weighted-Essentially-Non-Oscillatory (WENO) scheme²³, and the specific implementation details are presented in Kokkinakis et al.²⁰.

We briefly mention below the *enhanced* WENO spatial reconstruction characteristics in the framework of CNS3D. According to a transformation function, the local reconstruction stencils are normalized per variable, according to a transformation function²⁰. The transformation normalizes the candidate stencils so that the entire stencil’s maximum value becomes equal to one. The minimum value takes a positive and nonzero value, and the range scales to the maximum. The normalization of the total stencil values per variable prevents negative WENO smoothness indicator values, reduces the numerical dissipation and simplifies applying the proceeding step. In addition, the enhanced WENO scheme employs a modified version of the relative total variation (TV) limiting procedure of Taylor et al.²⁴ for the optimization of the non-linear error. Specifically, a TV limiting procedure for each candidate stencil is used to determine the maximum TV stencil value and the maximum TV ratio between the candidate stencils. If both values are below a threshold, then the linear WENO weights are used. The above procedure reduces both the computational cost associated with calculating the non-linear weights and the numerical dissipation. Moreover, when the non-linear WENO weights are calculated, these are modified according to the mapped WENO (WENO-M) approach by Henrick et al.²⁵ that increases the accuracy by achieving an optimal order near critical points.

Lastly, CNS3D uses a second-order central scheme to discretize the viscous terms. The solution is advanced in time using a five-stage (fourth-order accurate) optimal strong-stability-preserving Runge-Kutta method²⁶. CNS3D has been extensively validated against experimental and numerical results⁶.

III. MODELING OF ROCKET EXHAUST GASES

Below, we present the physical properties used in the rocket plume simulations, including the combustion chamber pressure and rocket fuel, and estimate the exhaust properties. Furthermore, we show the rocket trajectory and the variation of the atmospheric conditions with the altitude considered in this study.

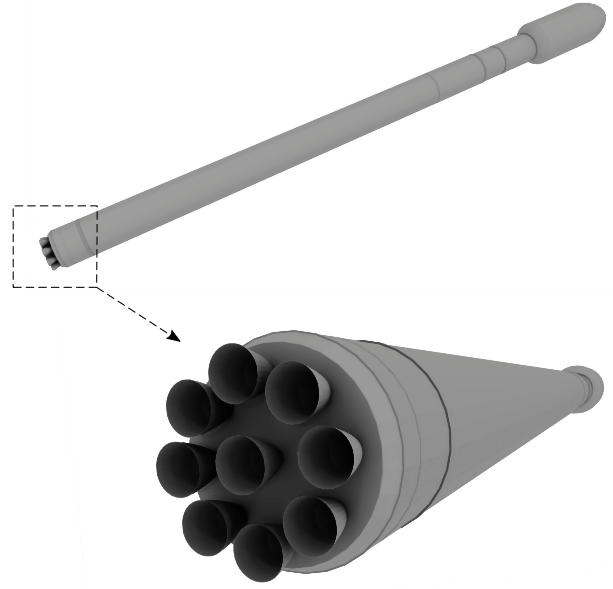


FIG. 1. Illustration of the considered rocket design highlighting the nozzles arrangement considered.

A. Rocket nozzle exhaust properties

The rocket nozzle exit conditions are calculated according to the NASA-GLENN “Chemical Equilibrium with Applications”²⁷ (CEA) computer program^{28–30}. One of the built-in applications includes calculating the rocket’s theoretical performance. CEA is used to calculate the chemical equilibrium product concentrations from any set of reactants and determine the thermodynamic and transport properties of the product mixture.

The assumed rocket properties are as close to typical values of modern-day rockets – such as the Falcon 9 – that employ solid rocket fuel. The rocket ground surface and vacuum, produced by nine nozzles, are 7,607 kN and 8,227 kN, respectively.

The nozzle exit diameter is taken as $d_e \approx 0.9304$ m, while the nozzle expansion ratio (nozzle exit to throat area) is assumed to be 16. Eight of the nozzles are arranged along a circular ring of radius 1.421m and spaced evenly every 45° , while the ninth nozzle is located at the centre of the ring. The latter is considered positioned on the same plane normal to the axial direction as the outer nozzle exits as Fig. 1.

The combustion chamber pressure is assumed to be $p_c \approx 9,721$ kPa (or 95.945 atm). The assumed rocket propellant (fuel) is RP-1 and liquid oxygen (LOx) is the oxidizer. The RP-1 capacity of the first stage is assumed to be ~ 123.57 t, while its LOx capacity ~ 287.43 t; it results in an RP-1 to LOx ratio of 1:2.326.

Using the above values CEA returns a specific impulse of $I_{sp} = 315.2$ sec. Therefore, the “equivalent” (or effective) exhaust gas velocity is estimated to be $u_e = I_{sp} * g_0 \approx 3,091$ m/s, where the earth’s gravitational acceleration is assumed constant and taken equal to $g_0 = 9.80665$ m/s². The velocity u_e is essentially the exhaust gases at the nozzles orifice/exit mea-

u_e (m/s)	ρ_e (kg/m ³)	p_e (Pa)	T_e (K)
3091.056	0.108	68,550.4	1,797

TABLE I. Flow properties at the rocket nozzles exit.

	CO	CO ₂	H	H ₂	H ₂ O	OH
x_j	0.32126	0.185	0.00015	0.15616	0.3374	0.00002
y_j	0.383	0.34543	7.2E-06	0.01323	0.2583	2.165E-05

TABLE II. Mole and mass fractions composition of the combustion products at the rocket nozzles exit.

sured relative to the rocket. In the Eulerian frame-of-reference simulations, the nozzle exits are modeled as (supersonic) inlets to the computational domain with the velocity above prescribed. Other properties of the exhaust gases at the nozzle exit required for the numerical simulations are summarized in Table I.

The mole-fraction, x_j , of each j -th combustion product at the nozzle exit is defined as:

$$x_j = \frac{n_j}{n_{tot}} \quad (13)$$

where n_j is the amount of a constituent (expressed in moles). The mole-fraction is converted to mass-fraction, y_j , as follows:

$$y_j = x_j \frac{\mathcal{M}_j}{\sum_i x_i \mathcal{M}_i} \quad (14)$$

The combustion products mole and mass fractions are summarized in Table II.

Note that other combustion products (e.g., HCO, HO₂, H₂O₂, O, COOH, O₂) are assumed to have been consumed from the nozzle throat to the nozzle exit – their molar/mass fractions are considered to be equal to zero.

B. Rocket trajectory

The assumed rocket launch trajectory is estimated using the captured telemetry data directly from SpaceX's webcast video feed of the Thaicom-8 launch mission. For reference, the captured data are plotted in Fig. 2.

The trajectory properties of the rocket can differ depending on the payload weight and altitude. Therefore, the simulations herein are only indicative. Moreover, we are interested only in the first stage of the launch, since above 70 km, the flow begins to become rarefied, and the fluid continuum assumption no longer remains valid, as we show below. We consider the Knudsen number, a dimensionless number defined by the ratio of the mean free path length of the molecules, λ , to a representative physical length scale, L , i.e., $K_n = \lambda/L$. The mean free path can be obtained according to,

$$\lambda = \frac{1}{\sqrt{2}n\pi d^2}, \quad (15)$$

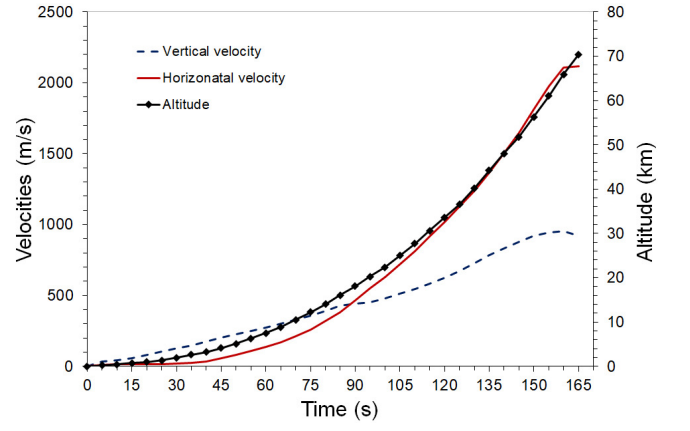
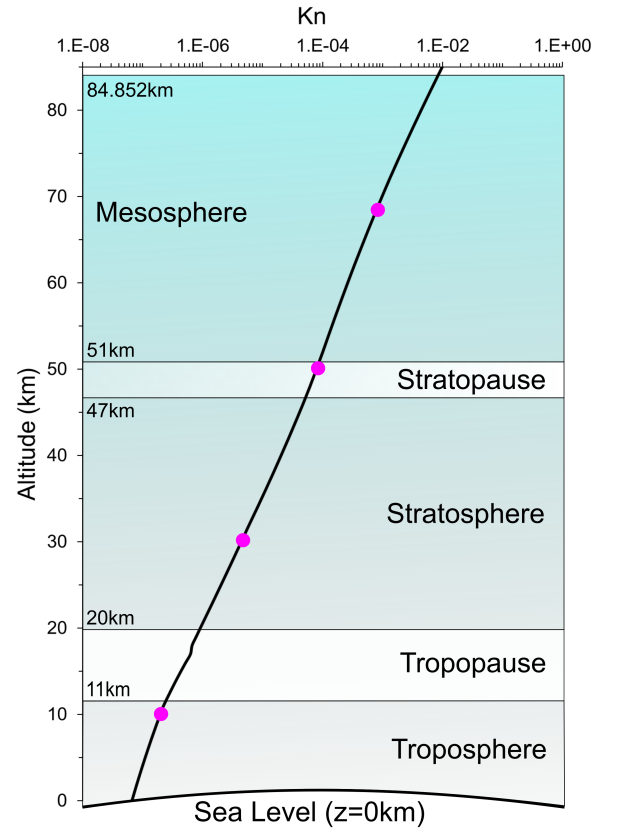


FIG. 2. Assumed rocket launch trajectory.

FIG. 3. Variation of the Knudsen number (K_n) with altitude using the rocket nozzle orifice diameter ($L \equiv d_e$) as the characteristic physical length scale; magenta colored circles indicate altitudes considered.

where d is the average particles diameter and n is the particles numerical density, taken from the atmospheric model. Note that $n = N_A \times (\rho/\mathcal{M})$, where $N_A = 6.02214076 \times 10^{23}$ is the Avogadro constant, while below an altitude of 85 km, the composition of the air does not change significantly, and so a constant molecular weight of $\mathcal{M} = 28.9647$ g/mol is assumed. An average, constant value for the molecular diameter is $d = 3.78 \times 10^{-10}$ m³¹. If the characteristic length is

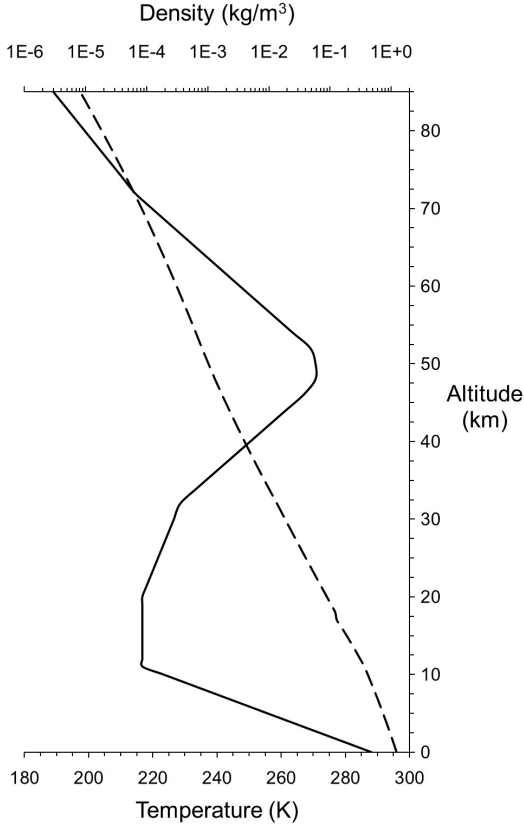


FIG. 4. Variation of the ambient atmospheric air temperature (solid line) and density (dashed line) with altitude.

taken equal to the diameter of the rocket exhaust nozzles, i.e., $L \equiv d_e = 0.9304$ m, then the Knudsen number at an altitude of 85 km is estimated to be less than $K_n \simeq 0.0098$, at the upper limit of the continuum fluid regime. Figure 3 shows the variation of the Knudsen number with altitude, using $L \equiv d_e$. At the highest altitude considered in this study ($z = 67$ km), the Knudsen number is estimated to be $K_n \simeq 0.000745$, well within the continuum fluid regime.

A body force acceleration is introduced and estimated according to $f_b(z) \equiv [u_{ar}(t_2) - u_{ar}(t_1)] / (t_2 - t_1)$, where t_2 and t_1 are the time of the rocket at the inlet and outlet altitudes of the computational domain in the axial direction, respectively, and u_{ar} is the corresponding axial velocity of the rocket.

C. Atmospheric properties with altitude

The 1976 U.S. Standard Atmosphere Model³² is used to obtain the mean properties of the atmospheric air at the various altitudes examined. For reference, the extracted ambient atmospheric air temperature and density versus altitude are plotted in Fig. 4. Note that the ambient pressure can be obtained from the perfect gas law equation, i.e., $p = \rho R_* T$ where a constant value for the atmospheric specific gas constant (R_*) can be assumed since the composition of the atmosphere does not change significantly below 85 km.

	N ₂	O ₂	Ar	CO ₂
x_j	0.78084	0.20946	0.009284	0.000416
y_j	0.75517	0.2314	0.0128	0.00063

TABLE III. Mole and mass fractions composition of the ambient atmospheric air below 85 km.

The altitude difference between the inlet (upper) and outlet (lower) boundary gives a gradient in the mean atmospheric air properties. This leads to a pressure difference, due to buoyancy effects caused by the Earth's gravity, which needs to be accounted for in Eqs. 2 & 3. The two are related via $g_0 \sim (dp/dz)/\rho$ (where z is the altitude); however, the mean atmospheric properties do not strictly adhere to the above equality, or otherwise $g_0 \approx (d\bar{p}/dz)/\bar{\rho}$ (where the overbar ($\bar{\cdot}$) denotes an averaged quantity). Thus, to maintain the hydrostatic flow equilibrium, the Earth's gravity is instead modeled in Eqs. 2 & 3 according to $f_b(z) \equiv g_0 = (d\bar{p}/dz)/\bar{\rho}$.

Regarding the composition of the atmospheric air, it does not vary significantly below 85 km and is thus assumed to remain the same at the various altitudes considered in this study. Table III depicts the values used in the simulations carried out.

D. Computational mesh

A cylindrical computational domain containing the developing rocket exhaust plume is used. Since the plume size changes with altitude both in the radial and axial directions, the domain size is increased accordingly to contain it. For the 10 km and 30 km altitudes, a radius of $l_r = 45$ m and an axial length of $l_z = 180$ m are employed, resulting in a domain that consists of 36.1 million cells. For the 50 km altitude case, the domain size is increased to $l_r = 180$ m and $l_z = 360$ m, comprising 114.3 million cells. For the 67 km altitude, the computational domain dimensions are $l_r = 360$ m, $l_z = 1,080$ m, and the grid consists of 188 million cells.

At the inlet, a square Cartesian grid with an edge size of 10 m and a resolution of 100 cells per edge is used to encompass the nine nozzle exit orifices for all considered altitudes. We use a diffuse interface for avoiding “step”-like features when mapping the circular exhaust jet orifice onto the Cartesian grid. Geometric progression extends the mesh in the radial direction, thus gradually increasing the size of the cells. On the opposite side, the (plume) exit plane comprises equal-sized cells in the axial direction. As a result, the cells at the inlet are initially clustered towards the plume region in the radial direction. Still, they are gradually evenly distributed while moving downstream in the axial direction to accommodate the expanding plume. The mesh resolution is initially equivalent to the Cartesian square grid along the axial direction. Employing a coarser axial mesh resolution at the inlet adversely impacts the accuracy of the expanding exhaust flow exiting the nozzles orifice and the interactions between the individual nozzle plumes. The computational cells' axial size does not increase more than tenfold from inlet to outlet to

	Mesh 1	Mesh 2	Mesh 3
No. cells $\times 10^6$	3.6	11.4	36.1
Mass (kg)	27.8	25.4	23.4
Heat (MJ)	36.1	32.8	30

TABLE IV. Total mass and thermal energy of atmospheric Nitrogen dioxide (N_2) heated above a temperature of 1,200 K at an altitude of 10 km for three different mesh resolutions.

ensure sufficient accuracy of the developing turbulent plume flow along the axial direction.

Although employing even finer grids would resolve finer turbulence structures, comparing the solutions obtained on the selected meshes shows that for the present analysis purposes, the dominant turbulent flow scale structures are adequately captured for all cases examined. Specifically, Table IV shows the results for the mass of the ambient atmospheric N_2 , heated above 1,200 K, as a result of the mixing occurring between the ambient air and hot rocket exhaust gases. Typically, the rate of thermal NOx emissions begins to climb at temperatures above $\approx 1,200 - 1,500$ K with significant amounts forming at temperatures above $\approx 1,800$ K³³⁻³⁵. A further temperature rise results in a rapid rise in NOx formation rate. Thermally produced NOx is the most significant contributor to such types of emissions.

As the mesh resolution increases, the mass of heated atmospheric N_2 decreases due to the reduction of numerical diffusion. The grid size has a lesser effect on the specific heat (heat per unit mass), which remains approximately similar between different grids.

IV. DISCUSSION

A. Emissions during rocket first stage launch

Using the flow properties (Table I) and species composition (Table II) at the rocket nozzle exits, as well as the rocket trajectory (Fig. 2), it is possible to calculate the total emitted rocket exhaust gases mass, e.g., per 1 km of altitude. The results are shown in Figure 5. In terms of total rocket exhaust mass emitted, the amount is negligible compared to 1 km^3 of ambient atmospheric air. Even at the higher altitudes of ~ 70 km, where the density of the ambient atmospheric air becomes very low, the total rocket exhaust mass emitted during the transverse of a 1km band is equivalent to a little less than 7% of a cubic kilometer of atmospheric air. Though this may seem surprising initially, the reason is the relatively short residence time of the rocket at the higher altitude bands. As the rocket accelerates and its speed increases to enter orbit, it transverses the higher altitude bands increasingly faster, despite the ground velocity becoming the dominant component (Fig. 2). Hence, the emission time decreases and, therefore,

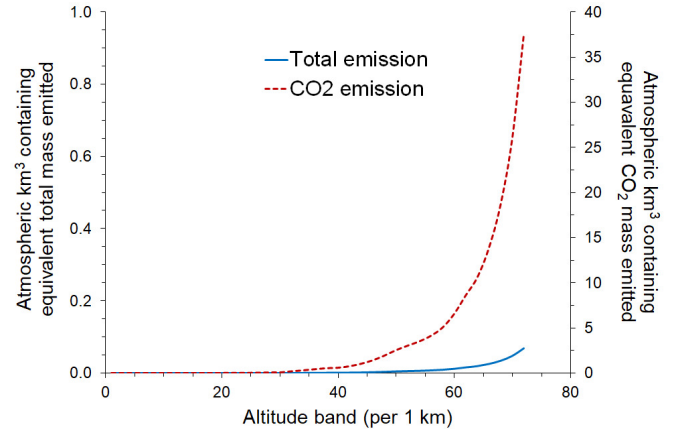


FIG. 5. Equivalent mass contained in square kilometers of local ambient atmospheric air emitted by rocket.

the total exhaust gases mass also emitted.

However, examining the total mass of CO_2 “injected” to the ambient atmospheric air at higher altitudes, we find that it becomes considerable. At about 43.5km, the total mass of CO_2 emitted by the rocket while increasing altitude by 1 km is equivalent to that contained in 1 km^3 of ambient atmospheric air at the same altitude. At an altitude of 70 km, the equivalent CO_2 mass emitted has climbed to an equivalent $\sim 26\text{ km}^3$ of local ambient atmospheric air, a significant value.

Perhaps even more crucially, the rocket exhaust mass-fractions of carbon monoxide (CO) and water (H_2O) are of a similar order as carbon dioxide (CO_2) (Table II), but are present in negligible amounts in the ambient atmospheric air. Therefore, these compounds’ emissions at high altitudes introduce an even more significant contribution/rise to the existing, if any, trace amounts already present. At this altitude in the mesosphere, water vapor does not stay in gas form and can sublime into ice particles, so how it spreads into the atmosphere is unclear. Regarding CO, the naturally occurring dominant local source at altitudes above 40 km is the photodissociation of CO_2 , whereas CO reactions with OH to form CO_2 are the most critical destruction pathways³⁶. However, the emissions of OH are relatively small compared to CO, as is the naturally occurring amounts in the ambient atmospheric air. Above 55km, the local destruction rate becomes small by comparison with the eddy diffusion rate (atmospheric turbulence) to lower altitudes³⁷, so it is expected that most of the CO emitted will eventually diffuse into the atmosphere. The CO_2 photolysis implies only minor changes to its vertical profile because photolytic loss is a small contributing factor in the CO_2 budget in the mesosphere and lower thermosphere (MLT)³⁸. Therefore, the CO and CO_2 emitted at the mesosphere are not expected to alter dramatically and eventually diffuse into the atmosphere primarily via eddy diffusion. According to past studies^{39,40}, the infrared emission caused by CO_2 is the primary cooling mechanism of the MLT. However, the exact time-scale and implications of the emitted rocket exhaust gases on the high altitude atmospheric chemistry remain uncertain.

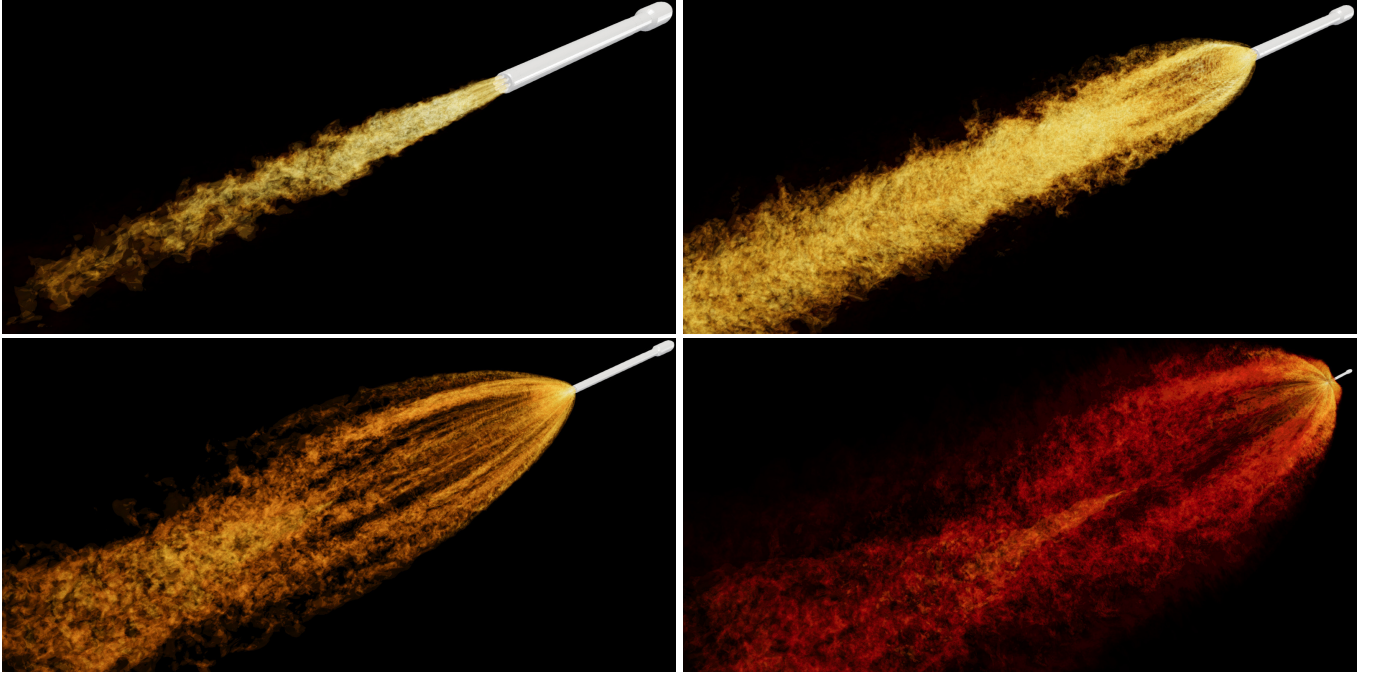


FIG. 6. Three-dimensional view of the rocket exhaust plume obtained at an altitude of 10 km, 30 km, 50 km, and 67 km from left-to-right then top-to-bottom. Temperature varies from 680 K (dark yellow) to 2,400 K (bright yellow). At 67 km the temperature contours down to 350 K (dark orange) are additionally shown.

B. High-resolution simulations

The present study assumes a high-Re behavior where the dissipation processes are controlled by the cascade to high wavenumbers and are not dependent on the Reynolds, Re , and Schmidt, Sc , numbers. The ILES simulations are conducted assuming that the Reynolds number is high enough so that the flow is beyond the mixing transition⁴¹, for the effect of the Schmidt number to become important. According to the experimental results^{41,42} and references, therein, the mixing transition corresponds to $Re \approx 10^4$. Therefore, inviscid ILES numerical simulations are carried out since the Reynolds number of the flow is significant, of order $\mathcal{O}(8)$ based on the considered rocket's nozzle exit flow properties and diameter. The effect of molecular diffusion and conduction on the flow are considered negligible in relation to the flow transport and turbulence and hence $\mu = \kappa = D_j = 0$ so Eqs. (5), (6) and (7) are not considered.

Four different altitudes above sea level are examined, namely 10, 30, 50 and 67 km. At an altitude of 10 km, the freestream ambient atmospheric pressure is approximately $p_\infty \approx 69.7\text{kPa}$, whereas the nozzle exit pressure determined in § III A is $p_e \approx 68.5\text{kPa}$. Therefore, the 10 km case is the only of the four cases examined for which the nozzle exit pressure ($p_e \approx 68.5\text{kPa}$) is relatively close –within the same order of magnitude– as the ambient air pressure ($p_\infty^{10\text{ km}} \approx 26.5\text{kPa}$), meaning the effects of the initial expansion remain relatively weak still. Moreover, since the ambient pressure is approximately equal to the nozzle exit pressure, i.e., $p_\infty^{10\text{ km}} \approx p_e$, the 10 km case is very near the optimum rocket altitude at

which a column-shaped exhaust plume forms, producing maximum efficiency. The ambient atmospheric pressure for the remaining three altitudes examined becomes increasingly lower; thus, the nozzle exit is under-expanded.

A snapshot of the rocket exhaust plume flow obtained from the high-resolution simulations is given in Fig. 6. The 10 km altitude case differs significantly from the other three under-expanded cases that simulate much higher altitudes since the initial expansion of the exhaust gases remains relatively weak. Perhaps the most significant difference is the relatively short distance from the nozzle orifices at which the exhaust plume temperature drops to below 700 K, which occurs due to the considerable turbulent mixing between the hot exhaust plume gases and the colder ambient air. Though the ambient air density at 10 km altitude is lower, it remains of the same order of magnitude as the exhaust gases and is thus able to absorb more heat, thus enhancing the rate of cooling.

Between the higher altitude simulations, from 30 km and above, a couple of essential differences can still be –qualitatively– discerned in Fig. 6. First is the size of the exhaust plume, both in terms of length (axial direction) and width (radial direction). Generally, as the altitude increases and the ambient atmospheric air pressure drops, the exhaust plume expands more axially and radially. More specifically, expansion waves originating at the nozzle orifice expand the rocket plume gases causing the pressure to drop and become equal to the ambient. At the same time, a slip surface forms, separating the exhaust gases from the atmosphere. The expansion fan reflects off this slip surface and re-expands part of the exhaust gases again, this time reducing the rocket plume pres-

sure below the ambient. As a consequence, the (outer) higher ambient pressure-flow “pushes” the (inner) re-expanded lower pressure plume gases inwards. In turn, the redirected radially inwards supersonic re-expanded gases eventually “collide” and begin to merge, forming a shock wave in the process that not only compresses the rocket exhaust plume gases but also increases their temperature; thus the noticeable and more prominent temperature contour surfaces originate at some distance downstream of the nozzle orifices, initially at the plume centerline.

C. Thermal NO_x formation potential

The mixing between the air and plume plays a critical role in the potential of –endothermic– chemical reactions at the plume. In atmospheric chemistry, NO_x is a generic term representing the total concentration of the various nitrogen oxides that are the most relevant for air pollution, particularly nitric oxide (NO) and nitrogen dioxide (NO₂), since the conversion between these two species is rapid in the stratosphere and troposphere. These gases contribute to the formation of smog and acid rain and affect the tropospheric ozone. The NO_x reduction is the most concerning issue today. Rockets can cause NO_x formation when the high-temperature reaction products they emit mix and heat the ambient atmospheric air. More specifically, thermal NO_x is produced when diatomic nitrogen and oxygen are present at high enough temperatures to undergo an endothermic reaction, high-temperature oxidation of N₂, thus making the various oxides of nitrogen. The two elements combine to form NO or NO₂.

To investigate the potential of the rocket exhaust plume in forming NO_x, we first examine the thermal energy carried by the exhaust plume. The top graph in Fig. 7 plots the thermal energy density, $\rho e = \rho c_v T$, carried by the exhaust plume of temperature 10 K above the local ambient atmospheric air, for the different altitude cases considered. Note that when referring to the exhaust plume, this comprises the rocket exhaust gases and the ambient atmospheric air, as the two mix downstream of the nozzle orifice due to the turbulent flow (molecular species diffusion is ignored). Regarding the simulations, the plot reveals that the domain sizes considered were large enough to contain the entire initial plume expansion process, as the convergence of the thermal energy density value nearing the domain exit suggests. As the altitude increases, the thermal energy increasingly decreases shortly after the nozzle exits. This is caused predominantly by the expansion of the exhaust gases that exit the nozzle at a much higher pressure than the local ambient atmospheric air, particularly for the latter three altitudes examined –from and above 30 km. As a result, the thermal energy is consumed to do pressure-volume work, and, therefore, less heat remains available for endothermic reactions to use and take place. On the other hand, the increased pressure-volume expansion work at the higher altitudes affects a much larger region of the local ambient atmospheric air, as the images in Fig. 6 also suggest.

Examining the formation of the NO_x, it is essential to measure the ambient atmospheric N₂ that is heated to a high

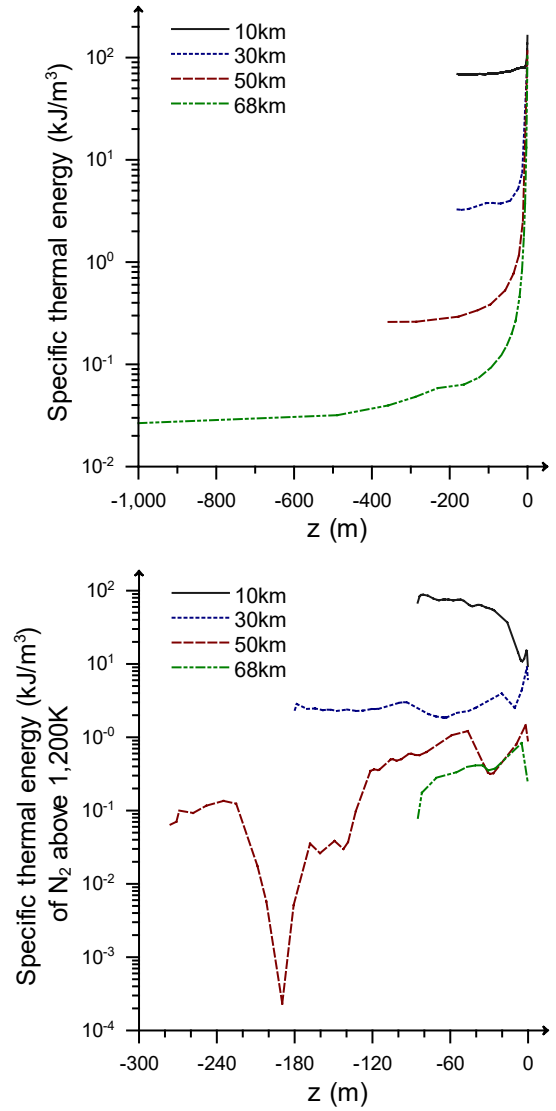


FIG. 7. Thermal energy density –averaged on the plane normal to the rocket axial direction– of the (top) rocket plume gas mixture above 10 K of the local ambient atmospheric temperature, and (below) atmospheric N₂ above 1,200 K.

enough temperature for thermal N₂ to form, as was earlier discussed. In the bottom graph of Fig. 7, the thermal energy density contained by N₂ at a temperature above 1,200 K is plotted versus the downstream distance from the nozzle exit.

Regarding the 10 km altitude case, the plot reveals that the thermal energy density of N₂ increases with distance from the nozzle exit; however, it abruptly stops just after 70 m from the nozzle exits. The former results from the intense mixing between the exhaust and atmospheric gases and are responsible for the –turbulent– heat transfer from the hot exhaust gases to the colder atmospheric air, thus N₂. On the other hand, the abrupt stop occurs due to the average plume temperature dropping below 1,200 K, the threshold value used. Note that the increased thermal energy density does not indicate N₂ rising in temperature. Rather, an increasing amount of N₂ is

heated to temperatures above 1,200 K as turbulence mixes the atmospheric air with the hot exhaust gases. While the mixing takes place, the mean temperature of the plume gas mixture decreases.

At 30 km altitude, the thermal energy density is almost an order of magnitude lower than the value obtained at 10 km. The initial decrease occurs due to the temperature drop caused by the exhaust gases undergoing expansion (pressure-volume work) immediately after the nozzle exits. After that, the thermal energy density remains almost constant up until the computational end of the domain – in this case, a distance of 180 m from the nozzle exits –, i.e., a considerable mass of the exhaust plume gas mixture remains above 1,200 K over that distance. Additionally, mixing with the freestream atmospheric air should gradually heat some N_2 above 1,200 K while cooling that already above. Therefore, the constant thermal energy density value implies that the thermal energy of N_2 heated above 1,200 K is in equilibrium with the thermal energy of N_2 , cooled towards or below 1,200 K. Overall, the total mass of N_2 heated above 1,200 K gradually grows downstream of the plume while its mean temperature drops. The slight rise observed between 60 and 90 meters from the nozzle exit is attributed to the aerodynamic heating caused by the under-expanded plume inner shock that forms, as was discussed in § IV B, and plays a critical role in the thermal energy equilibrium reaching an equilibrium.

At 50 km altitude, the thermal energy density is almost an order of magnitude lower than the corresponding value at 30 km due to the even greater initial pressure-volume expansion work done. Moreover, the value decreases downstream along the plume, which suggests that the resulting cooling of the plume due to the initial expansion was significant; the exhaust plume gases no longer carry sufficient thermal energy to maintain or heat enough N_2 above 1,200 K relative to the amount cooled as the two gradually mix. At ~ 290 m from the nozzle exits, the abrupt end in the specific thermal energy plot implies that the mean temperature of the plume gases mixture drops below 1,200 K –at least at the regions where the mixing between the atmospheric air and exhaust gases ensues. Again, the internal exhaust plume shock that forms causes a sudden rise in the thermal energy density between 190 and 230 meters, even more substantial than at 30 km, raising the plume gas mixture temperature significantly.

At 67 km altitude, the value of the thermal energy density remains, interestingly, at a similar order of magnitude as at 50 km. However, the expansion work is so significant that the mean temperature of the plume gases drops below 1,200 K within just ~ 80 m downstream of the rocket nozzle exits. This short distance becomes even more significant compared to the size of the exhaust plume formed –though the two are directly correlated.

While the thermal energy density axial profiles help reveal the dynamical behaviour of the potential NOx formation along the exhaust plume, it does not directly inform us of the formation potential in *absolute* terms. Table V shows the mass of N_2 heated above 1,200 K as well as the associated thermal energy by integrating across the computational domain. From the numbers quoted, it is expected that only those referring

	10 km	30 km	50 km	67 km
Mass (kg)	23.4	4.5	0.1	0.94
Heat (kJ)	30,000	5,500	125	1,150

TABLE V. Total mass and thermal energy of atmospheric Nitrogen dioxide (N_2) heated above 1,200 K.

to the 30 km altitude case are underestimated since the flow remained hotter than the threshold value of 1,200 K at the computational domain exit. Table V unequivocally shows that the potential for NOx formation is highest at the lower altitudes compared to higher altitudes despite the smaller overall plume size. This is primarily attributed to the lack of pressure-volume expansion work occurring at the lower altitudes where ambient atmospheric pressure is higher than the nozzle exit pressure (under-expanded nozzle case). Thus, nozzle exhaust gases remain at elevated temperatures that gradually mix and heat the surrounding atmospheric gases due to turbulence. Suppose all of the heated N_2 is assumed to react with oxygen particles to form nitrogen oxides (NOx), such as NO and NO_2 . In this case, the potential NOx produced would be equivalent to a concentration of $500 \mu\text{g}/\text{m}^3$ contained in approximately 0.047 km^3 of atmospheric air. Concentration levels even at this value are considered harmful to human health according to the World Health Organization (WHO) as it is associated with exaggerated/prolonged response to allergen challenges in asthmatics/atopics⁴³.

Note that the mass of the considered thermal NOx produced and discussed just above only accounts for that formed by the heated atmospheric air at a 10 km altitude and within 70 meters from the nozzle exit, a distance covered by the rocket within just ~ 1.5 sec. At altitudes below 10 km, not only is the air warmer –allowing for potentially more N_2 to be heated above 1,200 K– but the rocket travels slower, thus releasing more thermal energy for the same distance travelled. Consequently, the amount of NOx that can potentially be heated at high temperatures significantly increases at lower altitudes. For the first stage of the launch mission considered, the rocket took just under 70 sec to reach a 10 km altitude of the total 165 sec duration and 70 km altitude reached including main engine cut off (MECO). Even if the rate of NOx formation remained the same below an altitude of 10 km, enough thermal NOx could potentially be produced within this time to elevate NOx concentrations to $500 \mu\text{g}/\text{m}^3$ of over 2.1 km^3 of atmospheric air.

NOx can also combine with other pollutants in the atmosphere and create O_3 , a substance known as ground-level ozone – also considered a pollutant. Moreover, due to the presence of water vapour in the rocket nozzle exhaust and, potentially, in the atmospheric air – particularly at lower altitudes–, the nitrogen dioxide (NO_2) can react with the water (H_2O), forming Nitrous acid ($HONO$).

We also examined the potential of thermal NOx formation qualitatively due to the high-temperature rocket exhaust gases heating atmospheric N_2 and O_2 . We looked at the topological correlation between the high-temperature regions of the plume

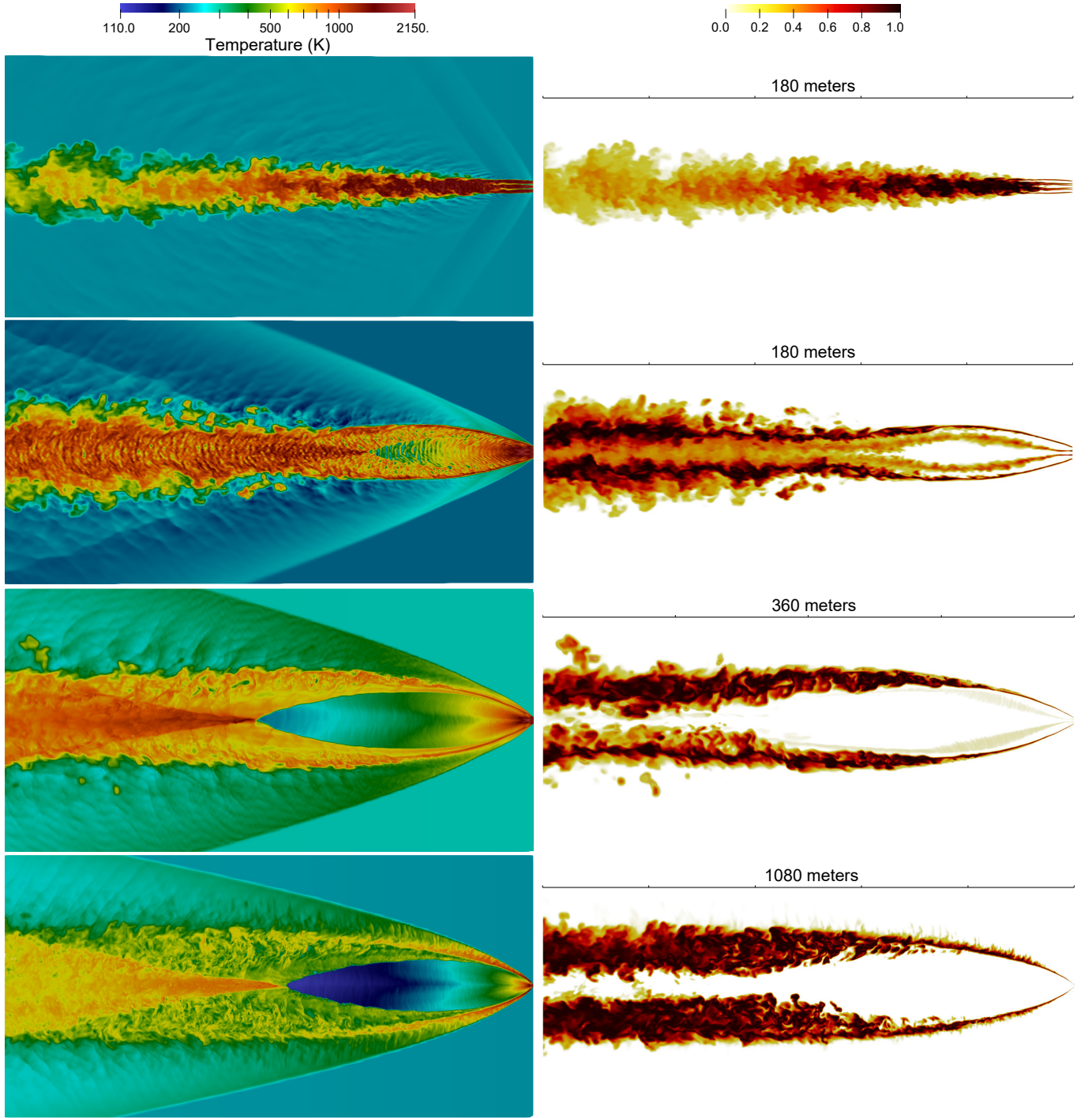


FIG. 8. Instantaneous temperature (left) and mixedness (right) contour plane at an altitude of 10, 30, 50 and 67 km (from top to bottom).

and the highly mixed areas in Fig. 8. The measure of mixing, or mixedness, between the ambient atmospheric air and the rocket exhaust gases is estimated according to,

$$\psi = \left| \left(\frac{y_{N_2, \infty} - y_{N_2}}{2y_{N_2, \infty}} \right) \left(\frac{y_{CO, e} - y_{CO}}{2y_{CO, e}} \right) \right|, \quad (16)$$

where “y” is the mass fraction of the specified species and the subscripts “ ∞ ” and “e” define the value of the property at the

ambient atmospheric air and the rocket nozzle exit, respectively. The former is assumed to contain no carbon monoxide (CO) while the latter no nitrogen (N₂). Therefore, $\psi = 1$ where equal masses of rocket exhaust gases and atmospheric air are present ($y_{N_2} \approx y_{CO}$), while $\psi = 0$ where only one or the other exists. Note that since we are dealing with gases, the two species will mix at a molecular level, i.e., are miscible.

As the individual exhaust plumes expand once they exit

their respective rocket nozzle (nine in total considered in this study), they collide with each other at supersonic speeds forming shock waves that heat the interior plume region. The temperature in some cases can exceed the original exhaust gases temperature at the nozzle exit, which from $T_e \approx 1,800$ K can rapidly climb up to or even surpass 2,150 K. Since the mixing with the atmospheric air is not yet substantial, the amount of N_2 heated to these high temperatures remains relatively tiny yet. Moreover, as the plume expands and gradually mixes with the cooler atmospheric air, its temperature drops. However, downstream, the atmospheric air pressure eventually becomes more extensive than that of the expanding plume, so the former “pushes” the latter inwards and towards the center region of the plume. Eventually, the inwards redirected opposite sides of the plume collide at supersonic speeds, forming an interior shock that emanates from the plume’s centre that causes significant heating.

It is evident in Fig. 8 that at an altitude of 10 km, the expansion of the exhaust gases is relatively weak and explains the relatively small drop in the thermal energy density obtained in Fig. 7. Two relatively weak shock waves can be seen to form in the atmospheric air that emanate from the vicinity near to the nozzle exits. The first shock wave occurs due to the initial weak expansion of the nozzle exhaust gases that collide with the supersonic freestream atmospheric air (rocket travels already faster than Mach 1 by this point). The second shock wave occurs due to the rapid re-collapse, merging, and transition to turbulence of the individual exhaust nozzles plumes. Despite the nozzle flow being under-expanded at the other altitudes too, the plume mixing at 10 km follows a distinctively different pattern. The maximum mixedness occurs shortly after the nozzle exits and at the interior/center region of the plume, rather than the “outer perimeter”. However, a distinct behaviour emerges as the mixedness obtained at the different altitudes are compared. At 30 km, some mixing occurring between the exhaust gases and the atmospheric air at the inner region of the plume near to the nozzle exits is still evident, which decreases further yet at 50 km and becomes practically negligible by 67 km. This can be explained by the decrease in atmospheric air mass-flux entering the plume interior from in-between the rocket nozzles as the ambient atmospheric air density decreases with altitude. As the altitude increases, less atmospheric mass enters the center/inner region of the plume to mix with the exhaust gases, thus reducing the mixedness. Therefore, the heat transfer from the exhaust gases to the atmospheric air – and therefore N_2 – occurs increasingly at the outer region of the plume with increasing altitude.

At 50 km and 67 km altitudes, most of the hot exhaust gases are located in the plume’s interior and are relatively cooled (below 1,200 K) until they mix with the ambient atmospheric air. This explains the relatively small amount of heated (above 1,200 K) N_2 mass estimated from the simulation results summarized in Table V. At 30 km altitude, the mixing at and around the plume center is more intense than the two higher altitude cases considered. At the same time, the temperature – despite the initial expansion – remains above 1,200 K, partly thanks to the inner plume shock, which raises the temperature sufficiently.

V. CONCLUSIONS

Improved understanding of rocket emissions requires modeling and simulation of fluid dynamics of rocket exhaust gases into the atmosphere, atmospheric chemistry changes due to gas emissions from rockets, and a better appreciation of the effects of different fuels. The insight into the gas dispersion into the atmosphere is crucial for appreciating the scale of pollution.

The present study considers a typical present-day rocket using RP-1 as the propellant that can generate $\sim 6,806$ kN of thrust via a total of 9 nozzles. It is shown that at an altitude of 70 km, the equivalent CO_2 mass emitted, is comparable to that contained in ~ 26 km³ of ambient atmospheric air at the same altitude, i.e., a significant value. Crucially, the rocket exhaust mass of carbon monoxide (CO) and water (H₂O) emitted are similar to carbon dioxide (CO₂) (Table II), while being present in negligible amounts in the ambient atmospheric air. Therefore, these compounds’ emissions at high altitudes introduce an even more significant contribution to the existing, if any, trace amounts already present in the ambient atmospheric air. According to^{39,40}, the infrared emission caused by CO₂ is the primary cooling mechanism of the mesosphere and lower thermosphere. However, the exact time-scale and implications of the emitted rocket exhaust gases on the high altitude atmospheric chemistry remain uncertain.

Concerning the formation of thermal Nitrogen oxides, NO_x, we found that it is potentially significant at an altitude of 10 km, since the exhaust gases do not undergo significant expansion. The simulations show that the cooling of the exhaust gases resulting from their expansion after the nozzle exits ($p_e > p_\infty$) is negated to a degree by the formation of two shock wave generating mechanisms inside the plume. One shock wave stems from the interaction between the individual nozzle plumes, expanding immediately after the nozzle exits. The second shock stems from the re-collapse of the merged plumes. Thus, the exhaust gas temperature remains high after the nozzle exit even at a 10 km altitude, transporting enough thermal energy to heat significant amounts of atmospheric N_2 above 1,200 K via eddy diffusion as the two mix due to turbulence.

Assuming the rate of NO_x formation during the rocket’s ascent to 10 km remains the same as at 10 km, sufficient NO_x could be produced over this time to pollute over 2 km³ of atmospheric air with a 500 $\mu\text{g}/\text{m}^3$ NO_x concentration. According to the world health organization (WHO), this would be at a level that becomes hazardous to human health⁴³.

At the higher altitudes examined, the ambient atmospheric pressure is much lower than the nozzle exit pressure, causing the exhaust gases to expand and cool significantly, thus reducing the thermal energy transported and eventually transferred to the ambient atmospheric air. At 30 km altitude, the inner plume shock raises the exhaust gases’ thermal energy enough to maintain the thermal energy balance between the N_2 mass heated above 1,200 K and that cooled towards or below. At 50 km altitude, the initial expansion (pressure-volume) work – immediately after the nozzle exits – cools the exhaust gases to the extent that despite the heating caused further downstream

by the inner plume shock, the rate of N_2 mass heated at above 1,200 K becomes in deficit relative to the cooled N_2 . Finally, at an altitude of 67 km, the initial exhaust gases expansion is so substantial that within a relatively short distance from the nozzle exits, no atmospheric N_2 can be heated at a temperature above 1,200 K.

We believe that the problem of atmospheric pollution caused by rocket launches is vital and needs to be addressed appropriately as commercial space flights, in particular, are expected to increase in the future. We currently plan to investigate, amongst others, the implications of the rockets' exhaust gases onto atmospheric ozone, and we will report these findings in a forthcoming paper.

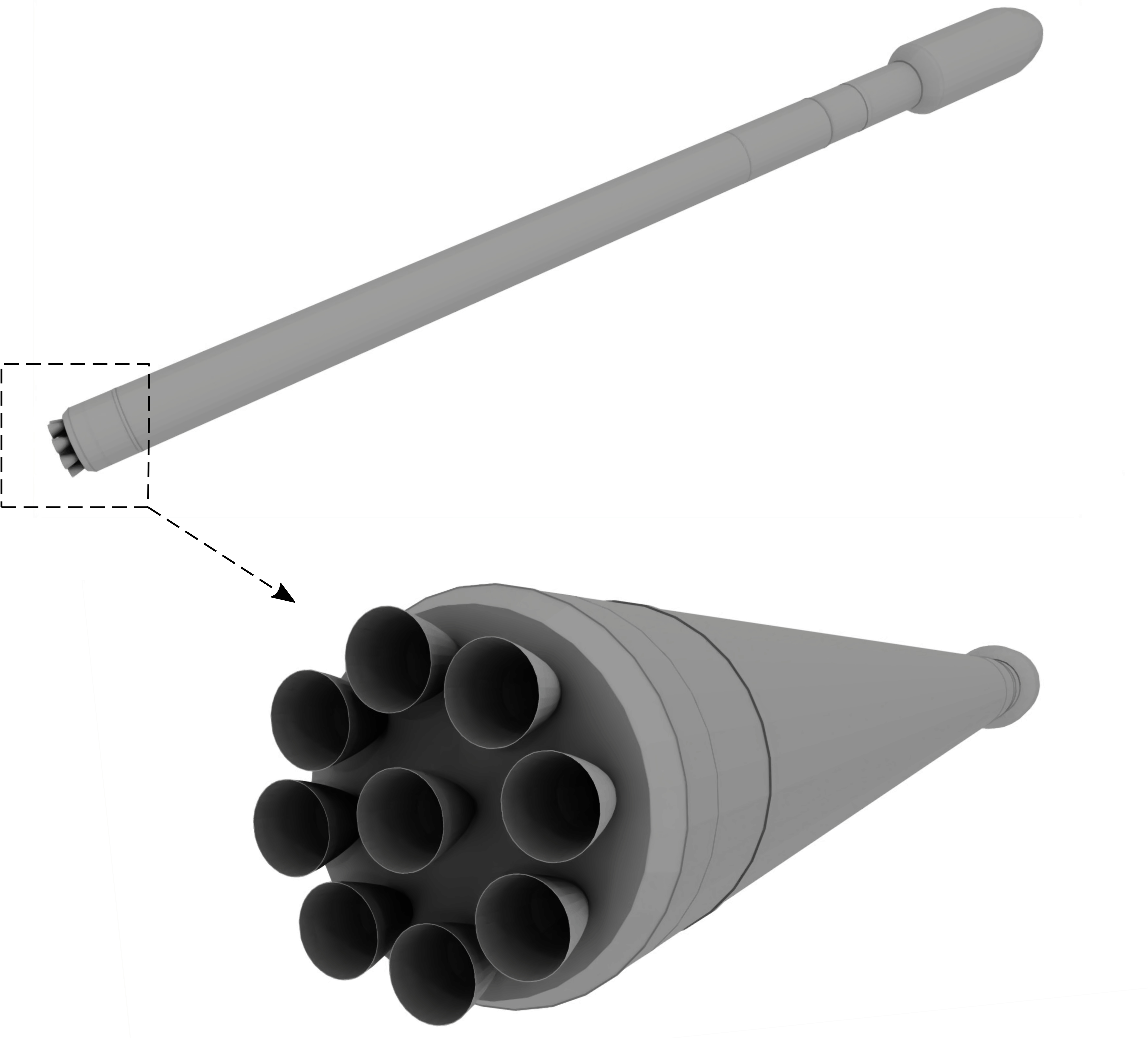
DATA AVAILABILITY

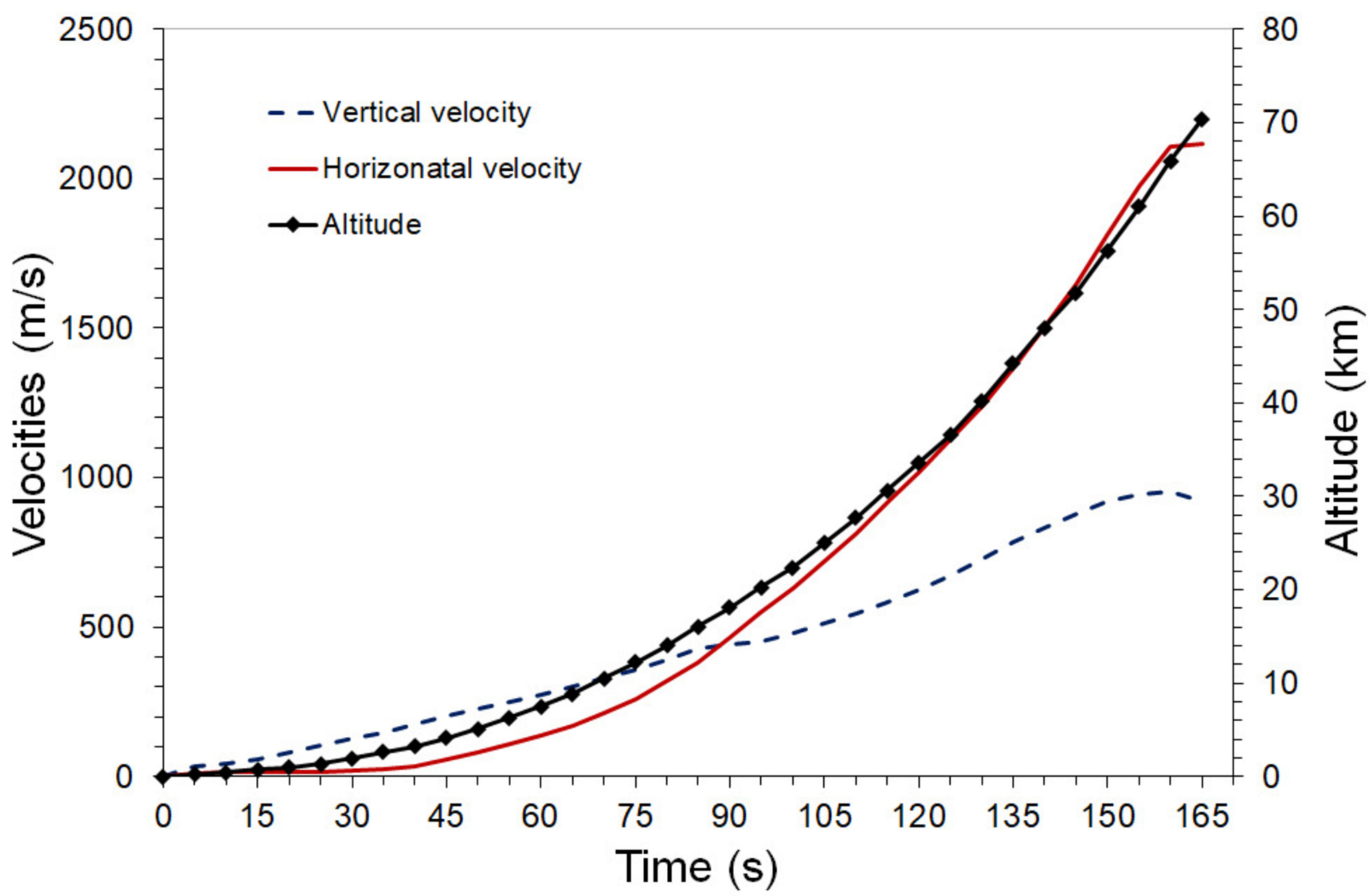
The data that support the findings of this study are available from the corresponding author upon reasonable request.

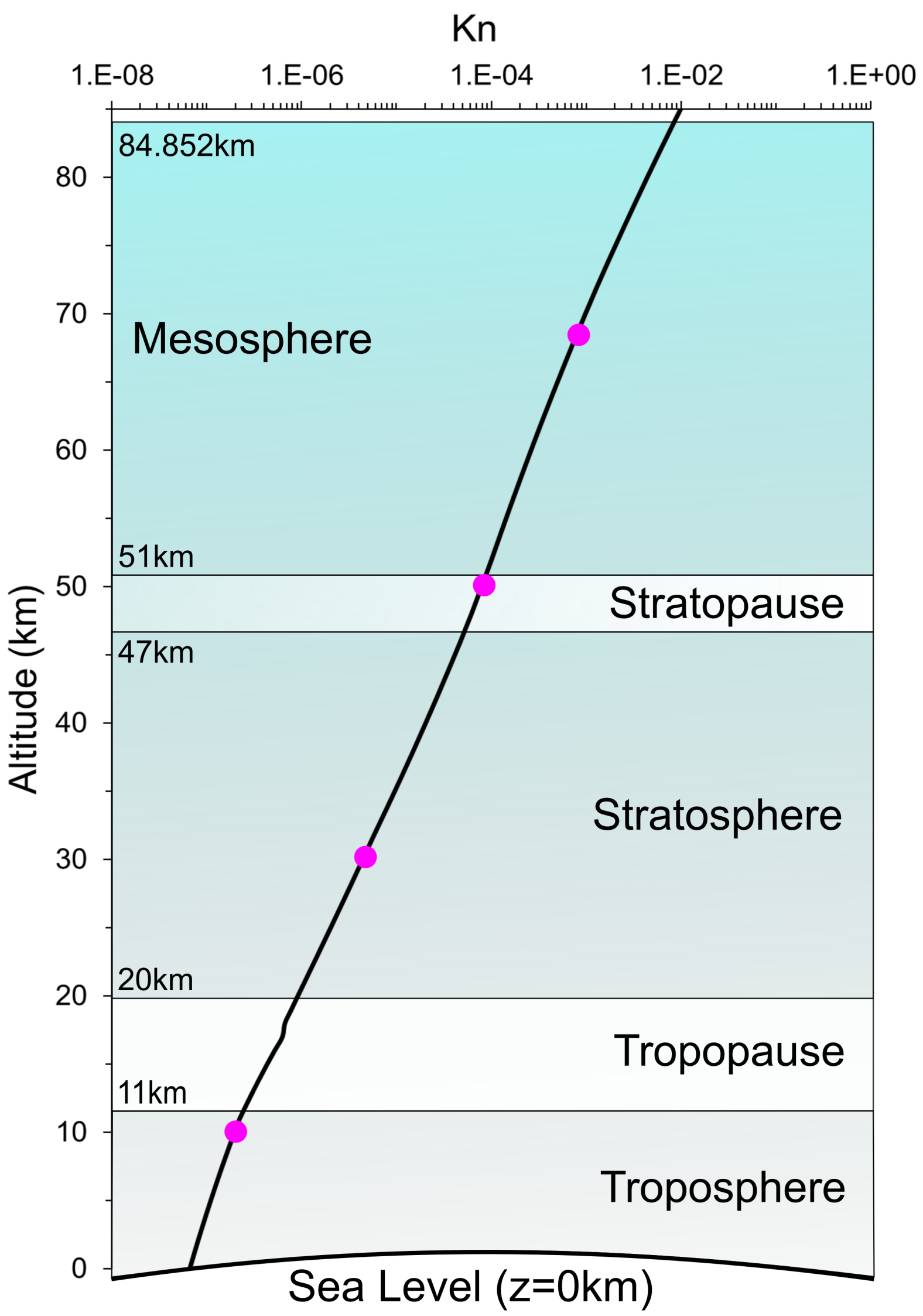
REFERENCES

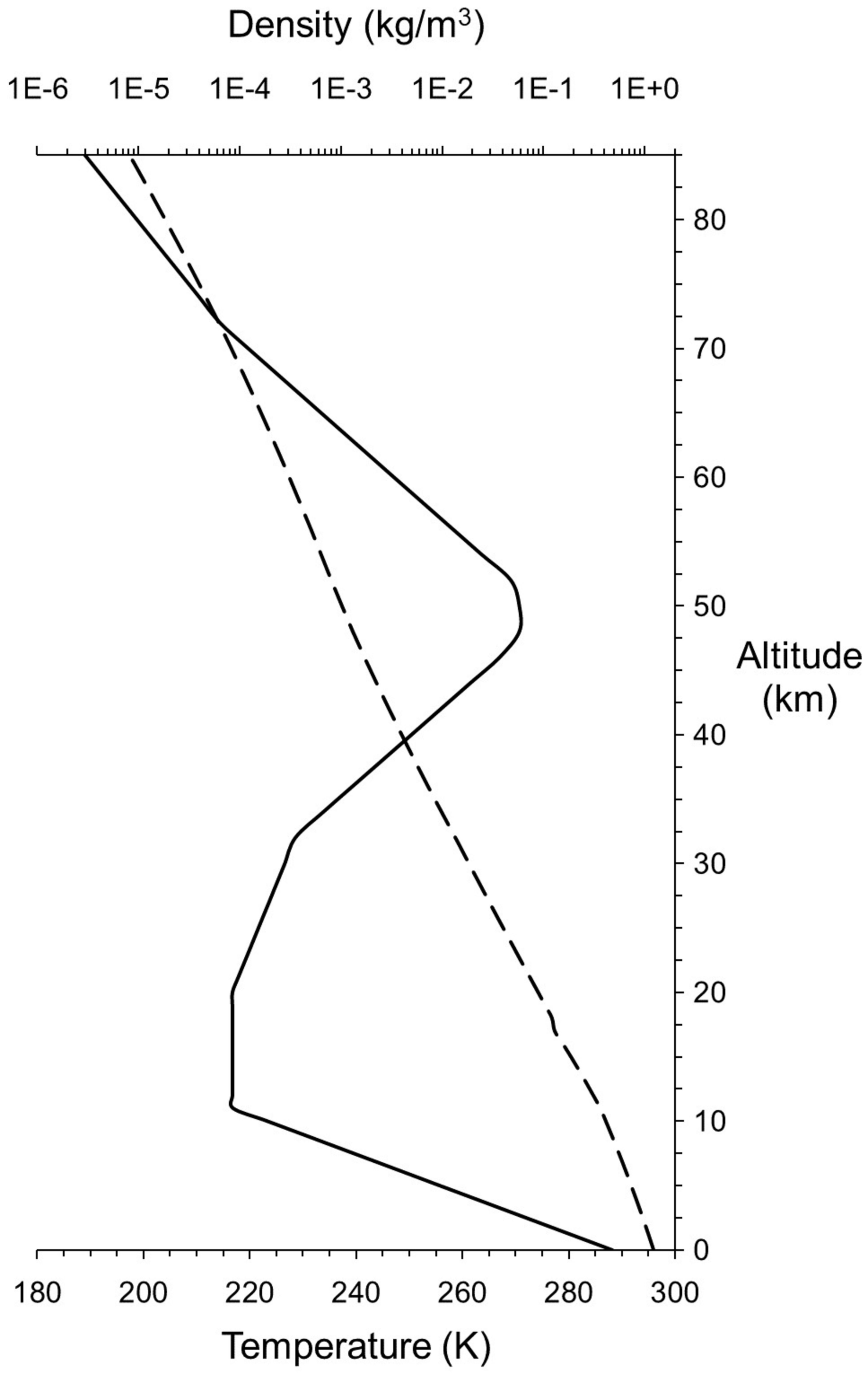
- ¹M. N. Ross and P. M. Sheaffer, "Radiative forcing caused by rocket engine emissions," *Earth's Future* **2**, 177–196 (2014), <https://agupubs.onlinelibrary.wiley.com/doi/pdf/10.1002/2013EF000160>.
- ²E. J. L. Larson, R. W. Portmann, K. H. Rosenlof, D. W. Fahey, J. S. Daniel, and M. N. Ross, "Global atmospheric response to emissions from a proposed reusable space launch system," *Earth's Future* **5**, 37–48 (2017), <https://agupubs.onlinelibrary.wiley.com/doi/pdf/10.1002/2016EF000399>.
- ³L. David, "How much air pollution is produced by rockets?" Tech. Rep. (Scientific America, 2017).
- ⁴N. R. Harris, D. J. Wuebbles, J. S. Daniel, J. Hu, L. J. Kuipers, K. S. Law, M. J. Prather, and R. Schofield, "Scenarios and Information for Policy-makers," in *Scientific Assessment Ozone Depletion : 2014. Global Ozone Research and monitoring Project - Report N° 55* (World Meteorological Organization (WMO), 2014) p. Chapitre 5:(62 p.).
- ⁵C. Voigt, U. Schumann, K. Graf, and K.-D. Gottschaldt, "Impact of rocket exhaust plumes on atmospheric composition and climate - an overview," in *EUCASS Proceedings Series - Advances in Aerospace Sciences*, Vol. 4, edited by Array (2013) pp. 657–670.
- ⁶D. Drikakis, M. Hahn, A. Mosedale, and B. Thornber, "Large eddy simulation using high-resolution and high-order methods," *Proceedings of the Royal Society A* **367**, 2985–2997 (2009).
- ⁷P. Tsoutsanis, I. W. Kokkinakis, L. Könözy, D. Drikakis, R. J. Williams, and D. L. Youngs, "Comparison of structured- and unstructured-grid, compressible and incompressible methods using the vortex pairing problem," *Computer Methods in Applied Mechanics and Engineering* **293**, 207 – 231 (2015).
- ⁸O. Zanotti and M. Dumbser, "Efficient conservative ADER schemes based on WENO reconstruction and space-time predictor in primitive variables," *Computational Astrophysics and Cosmology* **3**, 1–32 (2016).
- ⁹F. F. Grinstein, ed., *Coarse Grained Simulation and Turbulent Mixing* (Cambridge University Press, 2016).
- ¹⁰F. F. Grinstein, "Coarse grained simulation of convectively driven turbulent mixing, transition, and turbulence decay," *Physica D: Nonlinear Phenomena* **407**, 132419 (2020).
- ¹¹F. F. Grinstein, J. A. Saenz, and M. Germano, "Coarse grained simulations of shock-driven turbulent material mixing," *Physics of Fluids* **33**, 035131 (2021).
- ¹²W. Rider and D. Drikakis, "High resolution methods for computing turbulent flows," in *Turbulent Flow Computation. Fluid Mechanics and Its Applications*, edited by D. Drikakis and B. Geurts (Springer, Dordrecht, 2002) Chap. 2, pp. 43–74.
- ¹³L. G. Margolin, W. J. Rider, and F. F. Grinstein, "Modeling turbulent flow with implicit LES," *Journal of Turbulence* **7**, N15 (2006).
- ¹⁴F. F. Grinstein and C. Fureby, "On flux-limiting-based implicit large eddy simulation," *Journal of Fluids Engineering* **129**, 1483–1492 (2007).
- ¹⁵F. Grinstein, L. Margolin, and W. Rider, eds., *Implicit Large Eddy Simulation: Computing Turbulent Fluid Dynamics* (Cambridge University Press, 2007).
- ¹⁶W. J. Rider, "Effective Subgrid Modeling From the ILES Simulation of Compressible Turbulence," *Journal of Fluids Engineering* **129**, 1493–1496 (2007).
- ¹⁷W. J. Rider, "Building better (weighted) ENO methods," in *Computational Fluid Dynamics 2006*, edited by H. Deconinck and E. Dick (Springer, Berlin, Heidelberg, 2009).
- ¹⁸Z. Rana, B. Thornber, and D. Drikakis, "Transverse jet injection into a supersonic turbulent cross-flow," *Physics of Fluids* **23**, 046103 (2011).
- ¹⁹I. Kokkinakis and D. Drikakis, "Implicit large eddy simulation of weakly-compressible turbulent channel flow," *Computer Methods in Applied Mechanics and Engineering* **287**, 229 – 261 (2015).
- ²⁰I. Kokkinakis, D. Drikakis, K. Ritos, and S. M. Spottswood, "Direct numerical simulation of supersonic flow and acoustics over a compression ramp," *Physics of Fluids* **32**, 066107 (2020).
- ²¹E. F. Toro, M. Spruce, and W. Speares, "Restoration of the contact surface in the HLL-Riemann solver," *Shock Waves* **4**, 25 – 34 (1994).
- ²²E. F. Toro, *Riemann Solvers and Numerical Methods for Fluid Dynamics, A Practical Introduction*, 3rd ed. (Springer-Verlag Berlin Heidelberg, 2009).
- ²³D. S. Balsara and C.-W. Shu, "Monotonicity preserving weighted essentially non-oscillatory schemes with increasingly high order of accuracy," *Journal of Computational Physics* **160**, 405 – 452 (2000).
- ²⁴E. M. Taylor, M. Wu, and M. P. Martín, "Optimization of nonlinear error for weighted essentially non-oscillatory methods in direct numerical simulations of compressible turbulence," *Journal of Computational Physics* **223**, 384 – 397 (2007).
- ²⁵A. K. Henrick, T. D. Aslam, and J. M. Powers, "Mapped weighted essentially non-oscillatory schemes: Achieving optimal order near critical points," *Journal of Computational Physics* **207**, 542 – 567 (2005).
- ²⁶R. Spiteri and S. Ruuth, "A new class of optimal high-order strong-stability-preserving time discretization methods," *SIAM Journal on Numerical Analysis* **40**, 469–491 (2002).
- ²⁷<https://cearun.grc.nasa.gov/intro.html>.
- ²⁸S. Gordon and B. J. McBride, "Computer program for calculation of complex chemical equilibrium compositions and applications. Part 1: Analysis," Reference Publication NASA-RP-1311 (NASA, Glenn Research Center, 1994).
- ²⁹S. Gordon and B. J. McBride, "Computer program for calculation of complex chemical equilibrium compositions and applications. II. Users manual and program description," Reference Publication NASA-RP-1311-P2 (NASA, Glenn Research Center, 1996).
- ³⁰M. J. Zehe, S. Gordon, and B. J. McBride, "CAP: A computer code for generating tabular thermodynamic functions from NASA Lewis coefficients," Technical Publication NASA/TP-2001-210959/REV1 (NASA, Glenn Research Center, 2002).
- ³¹J. Moss, K. Boyles, and F. Greene, "Orion aerodynamics for hypersonic free molecular to continuum conditions," in *14th AIAA/AHI Space Planes and Hypersonic Systems and Technologies Conference* (AIAA, 2006) pp. 1–24.
- ³²P. M. Sforza, "Chapter 2 - Earth's atmosphere," in *Manned Spacecraft Design Principles*, edited by P. M. Sforza (Butterworth-Heinemann, Boston, 2016) pp. 13–46.
- ³³D. Leone and S. Turns, "Active chlorine and nitric oxide formation from chemical rocket plume afterburning," in *32nd Aerospace Sciences Meeting and Exhibit* (AIAA, 1994) <https://arc.aiaa.org/doi/pdf/10.2514/6.1994-788>.
- ³⁴J. Beer and M. Jacques, "Control of NOx by combustion process modifications," Tech. Rep. (MIT Energy Laboratory - MIT-EL 81-001, 1981).
- ³⁵Y. B. Zel'dovich, "The oxidation of nitrogen in combustion and explosions," *Acta Physicochimica URSS* **21**, 577–628 (1946).
- ³⁶S. C. Wofsy, J. C. McConnell, and M. B. McElroy, "Atmospheric CH₄, CO, and CO₂," *Journal of Geophysical Research* (1896-1977) **77**, 4477–4493 (1972).
- ³⁷P. F. Goldsmith, M. M. Litvak, R. L. Plambeck, and D. R. W. Williams, "Carbon monoxide mixing ratio in the mesosphere derived from ground-

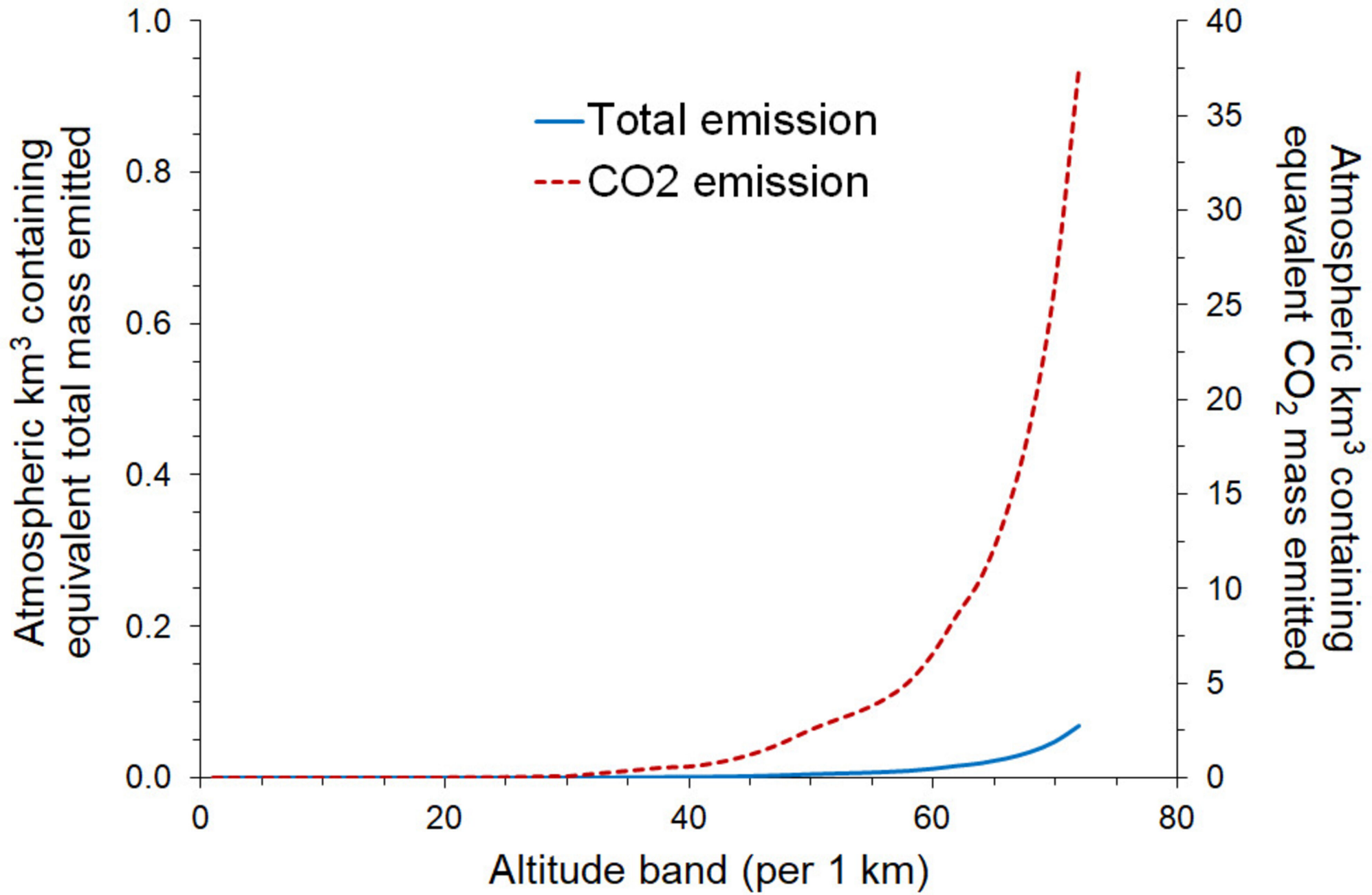
- based microwave measurements,” *Journal of Geophysical Research: Space Physics* **84**, 416–418 (1979).
- ³⁸R. R. Garcia, M. López-Puertas, B. Funke, D. R. Marsh, D. E. Kinnison, A. K. Smith, and F. González-Galindo, “On the distribution of CO₂ and CO in the mesosphere and lower thermosphere,” *Journal of Geophysical Research: Atmospheres* **119**, 5700–5718 (2014).
- ³⁹M. López-Puertas and F. W. Taylor, *Non-LTE Radiative Transfer in the Atmosphere* (World Scientific, 2001) p. 504.
- ⁴⁰M. G. Mlynczak, F. J. Martin-Torres, C. J. Mertens, B. T. Marshall, R. E. Thompson, J. U. Kozyra, E. E. Remsberg, L. L. Gordley, J. M. Russell III, and T. Woods, “Solar-terrestrial coupling evidenced by periodic behavior in geomagnetic indexes and the infrared energy budget of the thermosphere,” *Geophysical Research Letters* **35** (2008), 10.1029/2007GL032620.
- ⁴¹P. E. Dimotakis, “The mixing transition in turbulent flows,” *Journal of Fluid Mechanics* **409**, 69–98 (2000).
- ⁴²A. W. Cook and P. E. Dimotakis, “Transition stages of Rayleigh–Taylor instability between miscible fluids,” *Journal of Fluid Mechanics* **457**, 410–411 (2002).
- ⁴³D. J. Jarvis, G. Adamkiewicz, M.-E. Heroux, R. Rapp, and F. J. Kelly, “Nitrogen dioxide,” in *WHO Guidelines for Indoor Air Quality: Selected Pollutants* (World Health Organization, Geneva, 2010) Chap. 5, Available from: <https://www.ncbi.nlm.nih.gov/books/NBK138707/>.

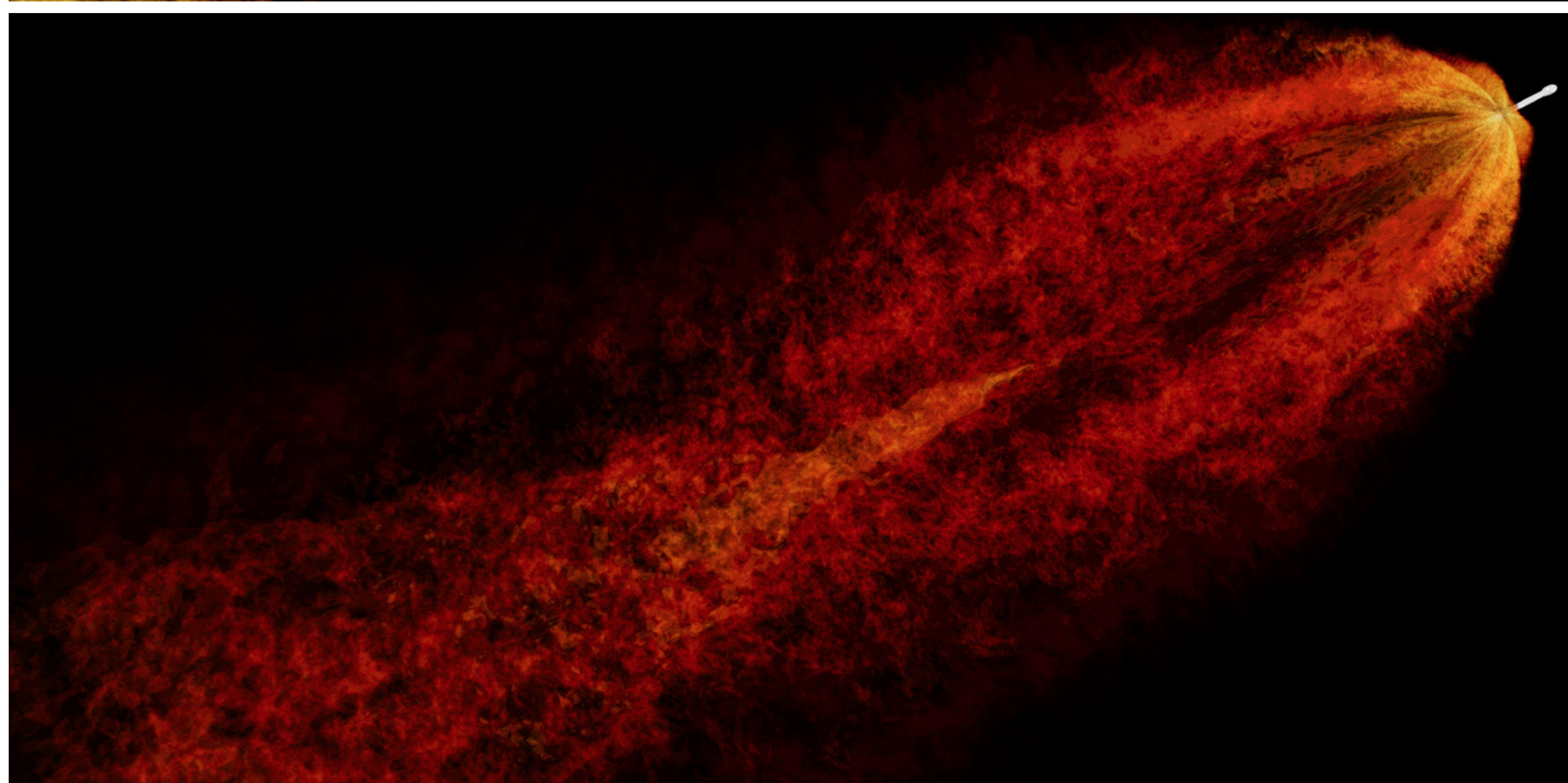
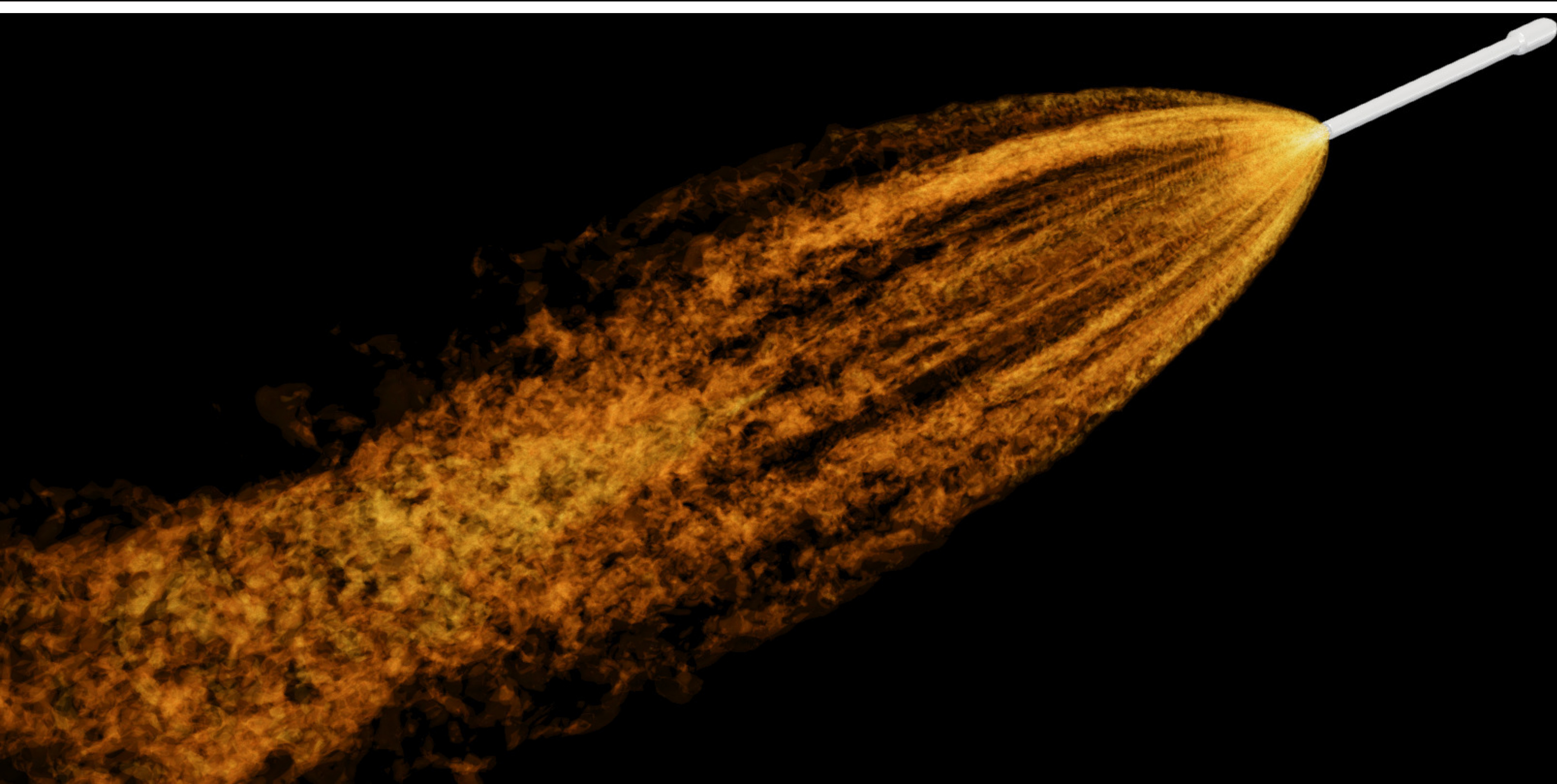
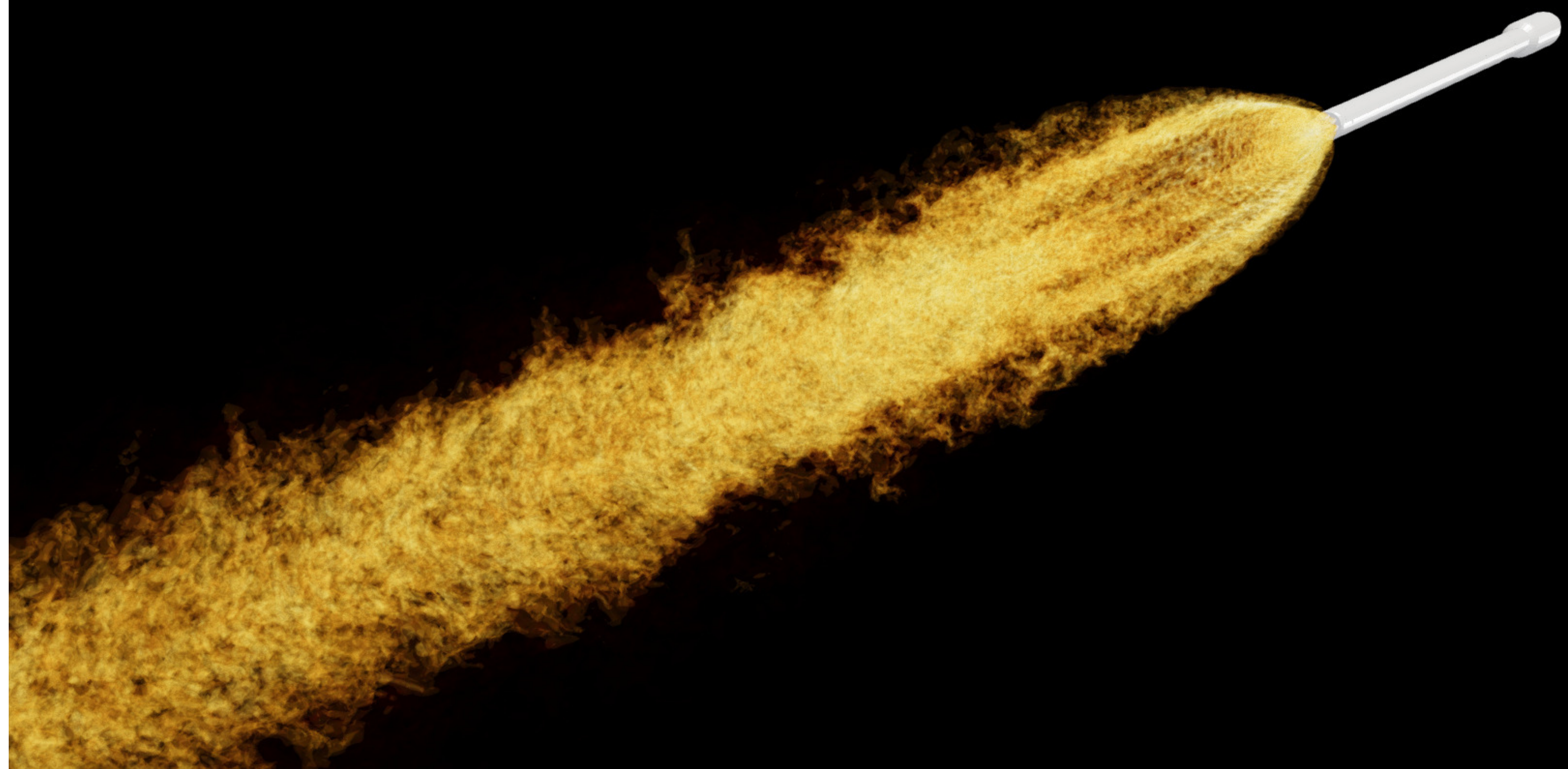


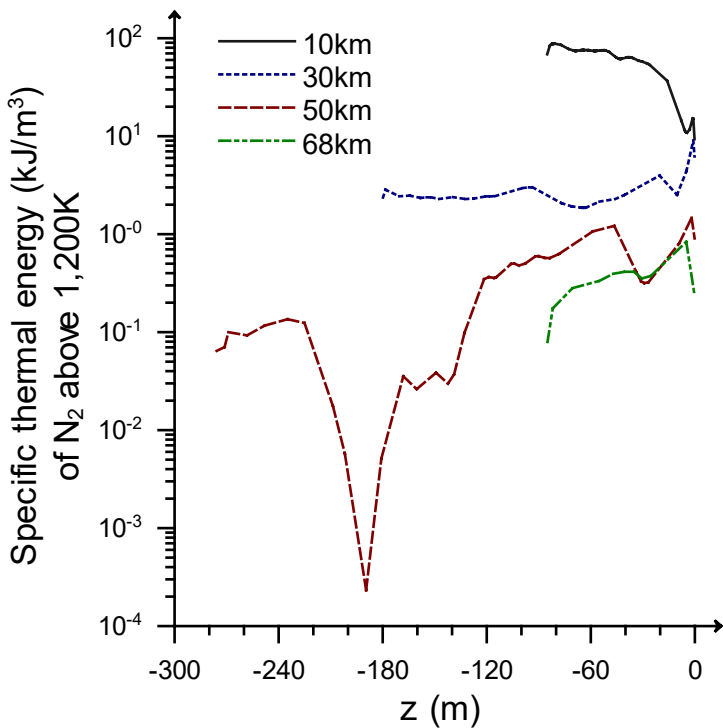
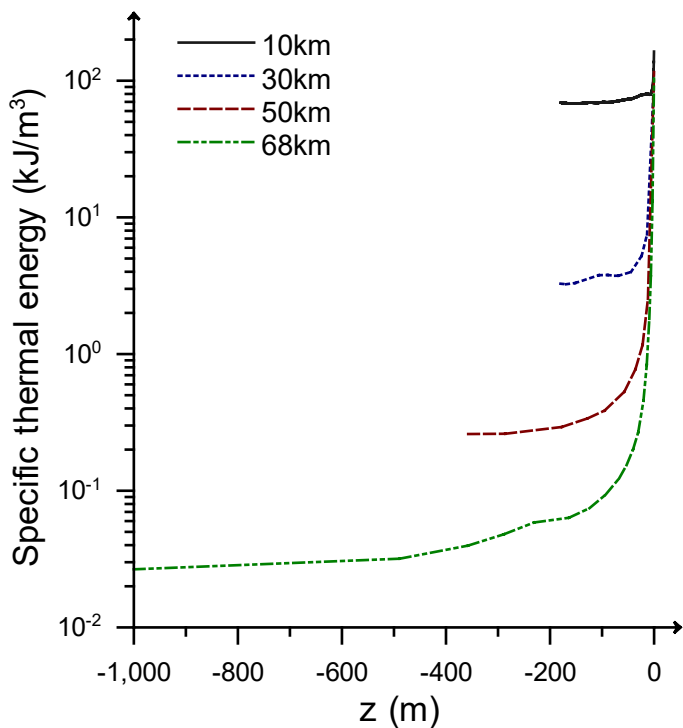


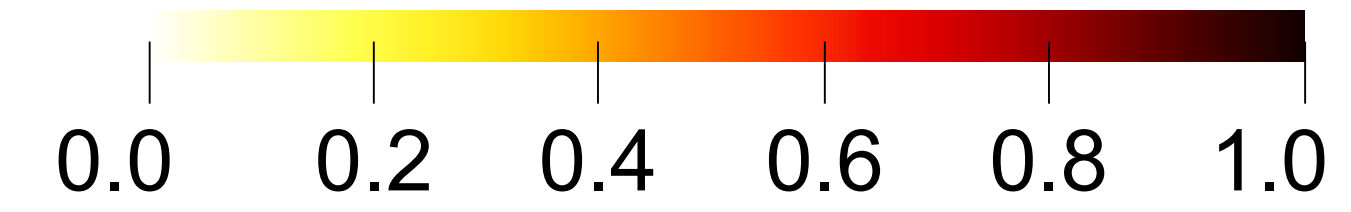
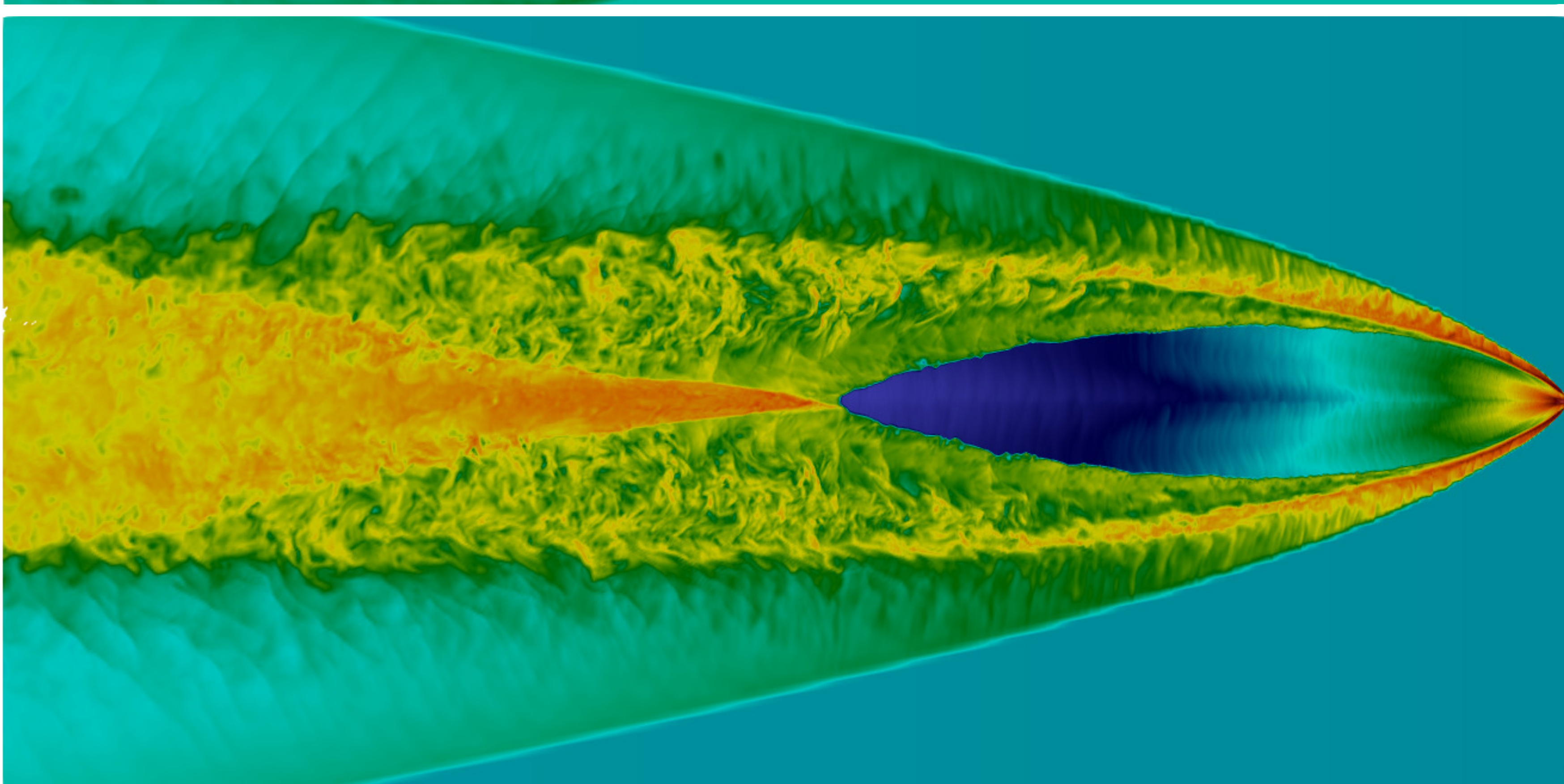
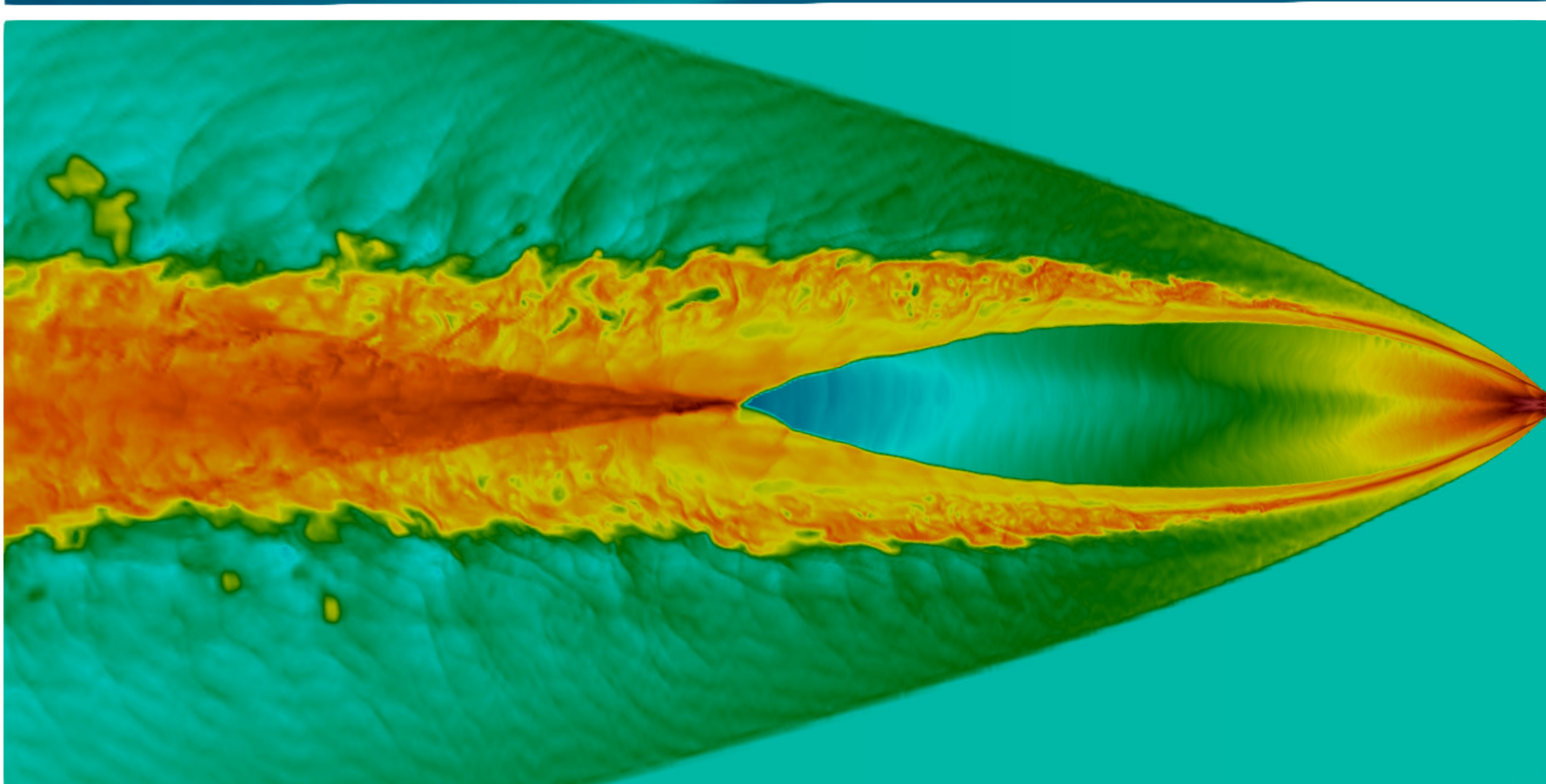
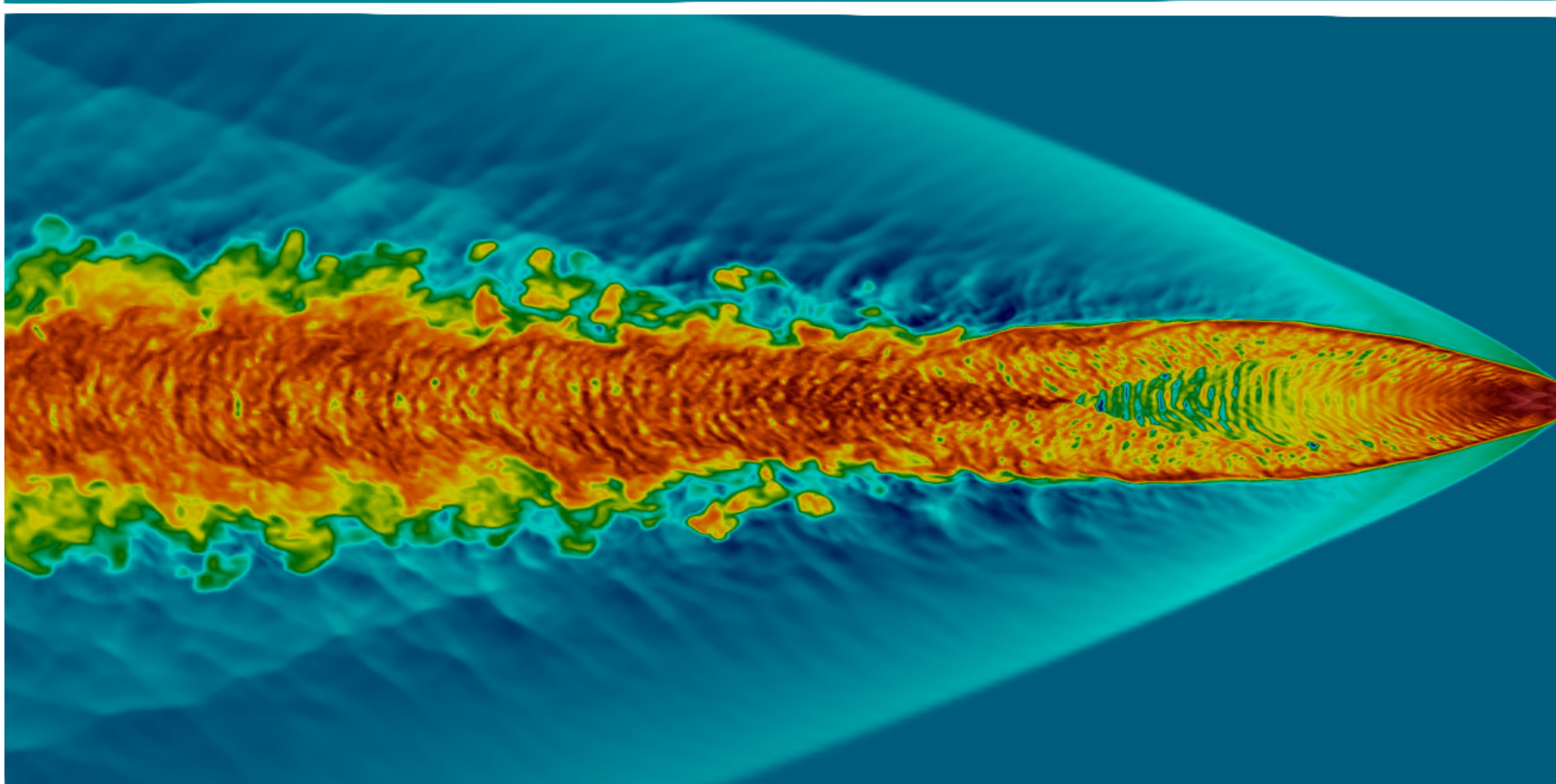
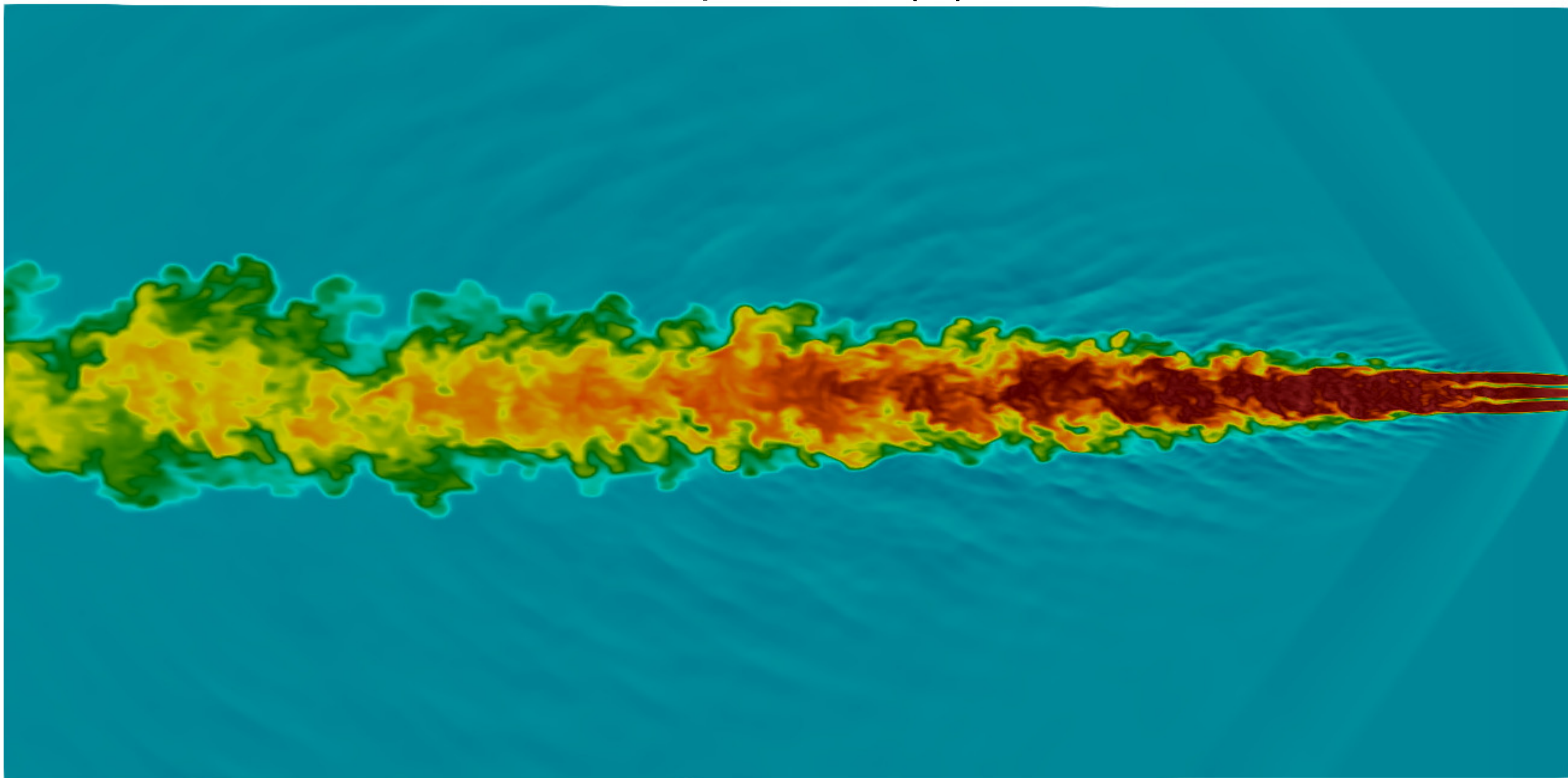
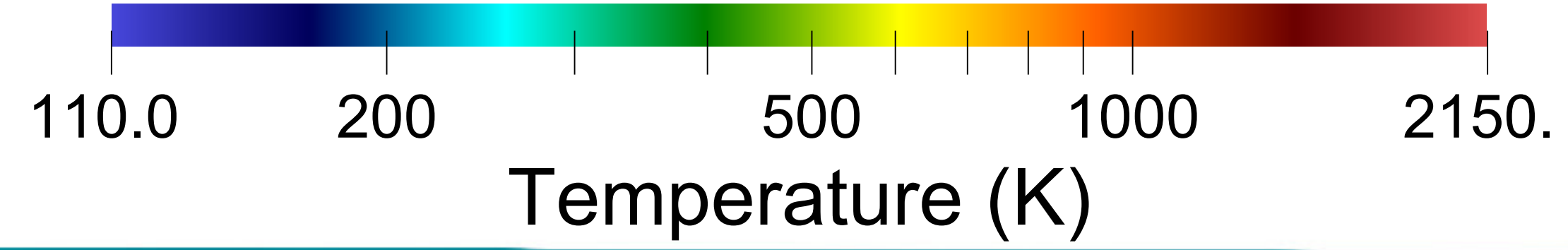




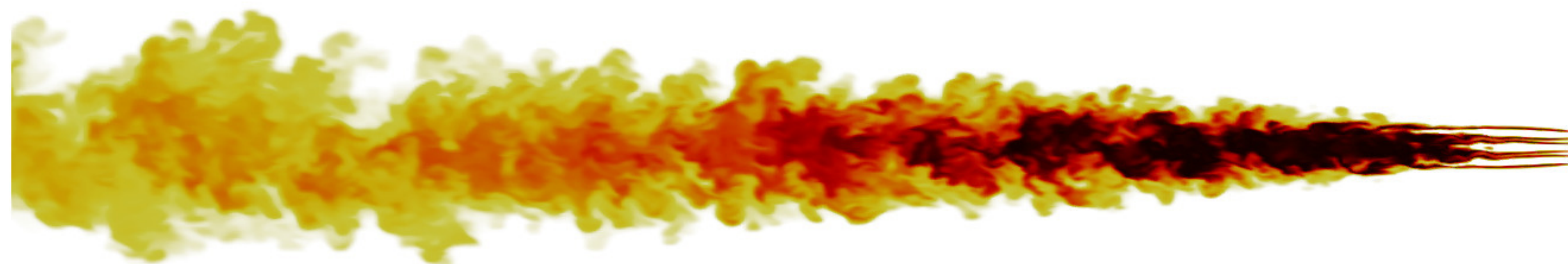




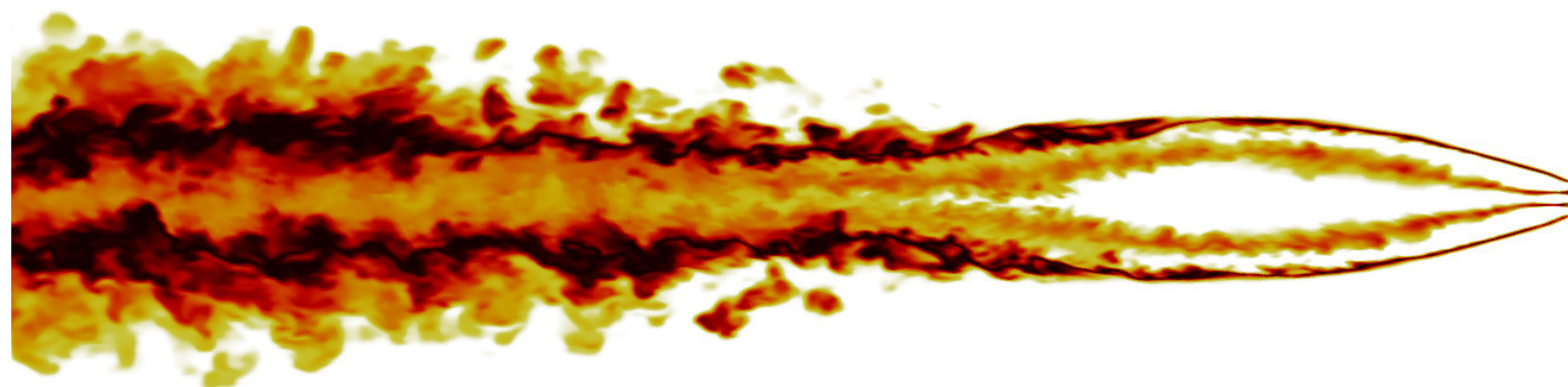




180 meters



180 meters



360 meters



1080 meters

